

INTERNAL REPORT #80

CALIBRATIONS OF THE VOYAGER LOW ENERGY TELESCOPES'  
RESPONSE TO HIGH COUNTING RATES

by

N. Gehrels

Space Radiation Laboratory  
California Institute of Technology  
Pasadena, California  
November 3, 1981



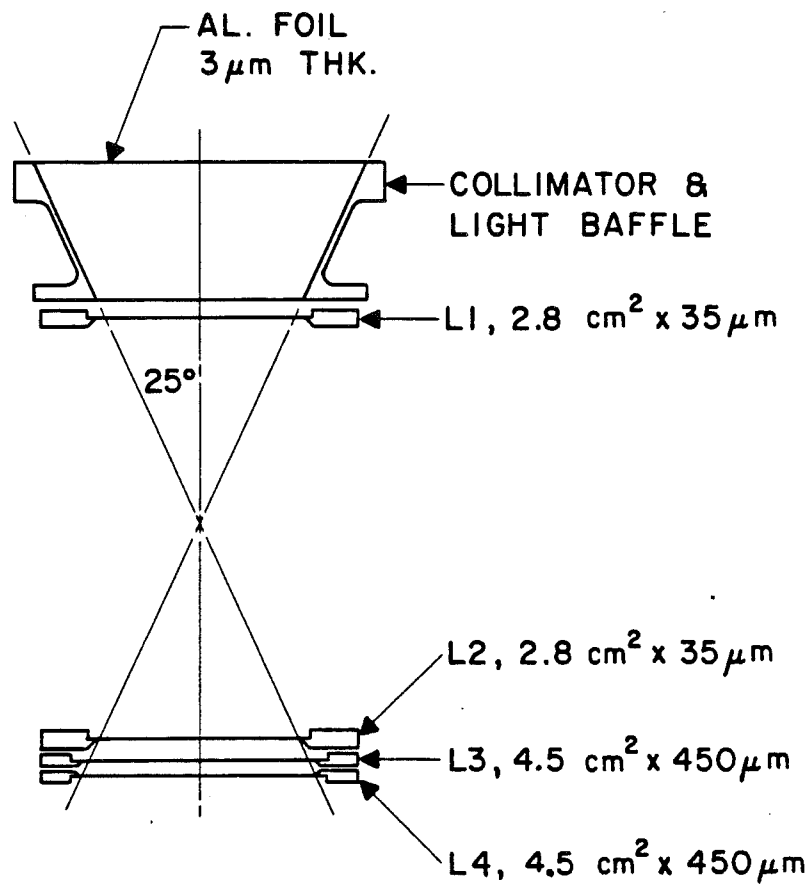
## Introduction

In high radiation environments, such as Jupiter's inner magnetosphere, several effects occur in the electronics of the Voyager Cosmic Ray Subsystem (CRS) that must be corrected for before absolute particle fluxes and energy spectra can be obtained from the data. These include discriminator threshold changes caused by baseline shifts at the output of the detector amplifiers and discriminator deadtime effects. In order to quantify and help understand these effects, the spare CRS instrument was calibrated in 1979 - 1980. The specific goal of the calibration was to measure the response of the Low Energy Telescopes (LETs) to oxygen and sulfur nuclei in the presence of high fluxes of protons and electrons. This report describes how the calibration was done and presents the results that were obtained. In addition, a short description is given of the LET configuration and logic. Calibration results and data that are not in this report are in a notebook labelled "LET Livetime Calibrations" in Room 207 (see A. C. Cummings). A summary of the calibration results is presented in the appendix of Gehrels *et al.* (1981). More general descriptions of the CRS investigation can be found in Stone *et al.* (1977) and Stilwell *et al.* (1979).

## LET Configuration, Timing, and Rates

A cross-section of a LET is shown in Figure 1. All detectors are silicon surface-barrier detectors with the following nominal cross-sections: Aluminum metallization ( $\sim 40 \mu\text{g}/\text{cm}^2$ ), n region ( $35 \mu\text{m}$  L1, L2;  $450 \mu\text{m}$  L3, L4), very thin p region, gold metallization ( $\sim 40 \mu\text{g}/\text{cm}^2$ ). When fully biased, the detectors have no dead layer aside from the metallization. The detector orientations and

**Figure 1**  
Cross-section of a LET.



LOW ENERGY TELESCOPE (LET)

biases are shown in Figure 2.

The LETs use a strobed coincidence logic triggered by detector L1. This means the following: The L1 discriminator starts a countdown timer which is called a one-shot. At the end of the countdown, the discriminator levels of all detectors are strobed (checked) and the established coincidence is compared to rate and pulse-height analysis conditions. The one-shot countdown time is set at  $\sim 4 \mu s$  which is shown in Figure 3 to be long enough, even for the extreme example of an event with a large signal in L1, causing an early discriminator, and a small signal in L2 that just exceeds threshold, causing a late discriminator. The L2 discriminator is also shown to have a delayed response of  $\sim 1 \mu s$  which is typical for small signals. If the required discriminators are up at the time of the strobe, a valid coincidence is established and the gates at the input of the pulse-height analyzers (PHAs), called the linear gates, are opened. (Open means connected to the PHA, closed means disconnected.) There can be as much as a  $2 \mu s$  delay between the strobe and the opening of the linear gates due to finite time requirements for testing the coincidence ( $\sim 1 \mu s$ ) and opening the gates ( $\sim 1 \mu s$ ). This delay plus the discriminator delay, the amplifier shaping time, and the one-shot time can result in the linear gates opening as much as  $\sim 9 \mu s$  after the event. An example of such a worst-case delay is shown in Figure 4. In order to keep the amplifier signals from reaching the linear gates before they open, the amplifiers are connected to the PHAs through a  $\sim 10 \mu s$  delay line. During the linear gate open time, a comparator compares the input signal level to the voltage across a reference capacitor, and controls the current flow onto the capacitor such as to keep the voltages equal. When the peak of the input signal is passed, the comparator shuts off, leaving the reference capacitor charged at the peak voltage. After the gate closes ( $\sim 10 \mu s$  after opening), the amount of charge on the capacitor is determined by measuring the time it

**Figure 2**

Detector orientations and bias configuration of a LET.

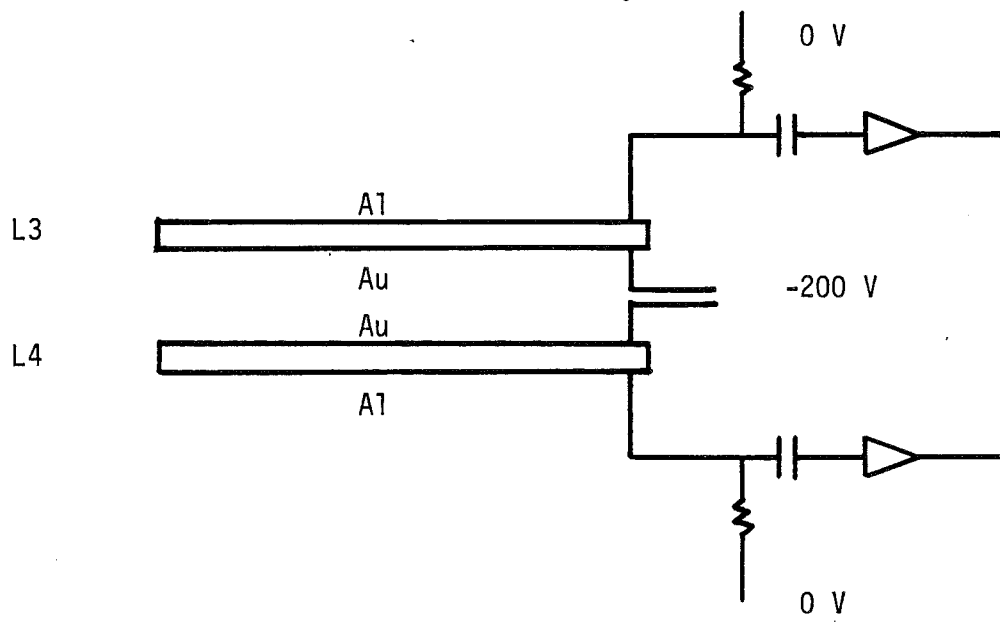
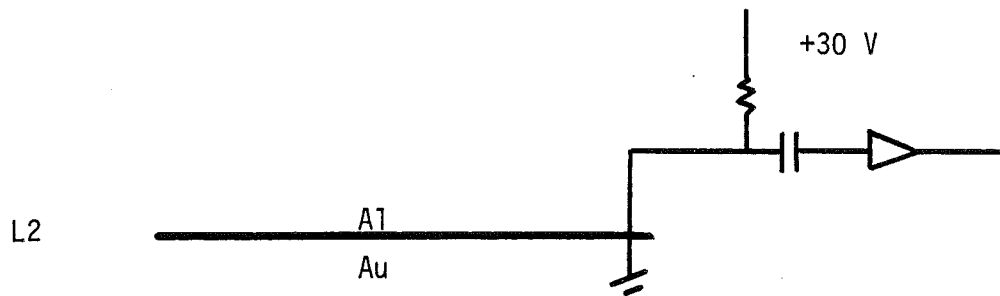
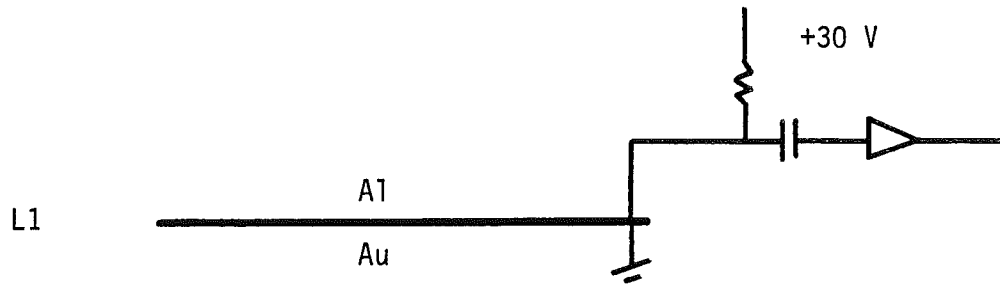




**Figure 3**

Timing diagram of an event with a large energy loss in L1 and a small energy loss in L2. Shown, from top to bottom, are the L1 amplifier output, the L1 discriminator state, the one-shot state (up means counting), the strobe, the L2 amplifier output, and the L2 discriminator state.

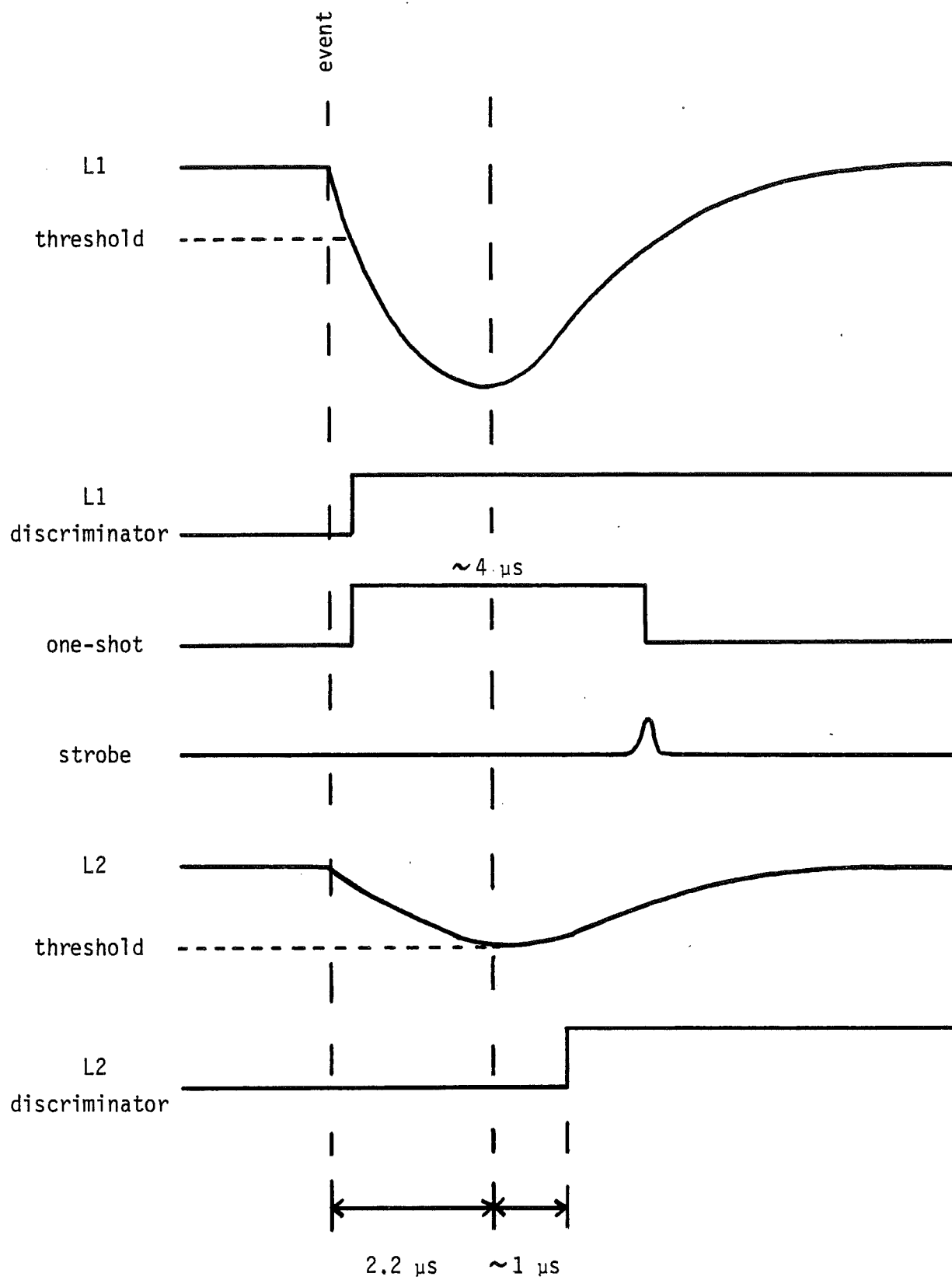
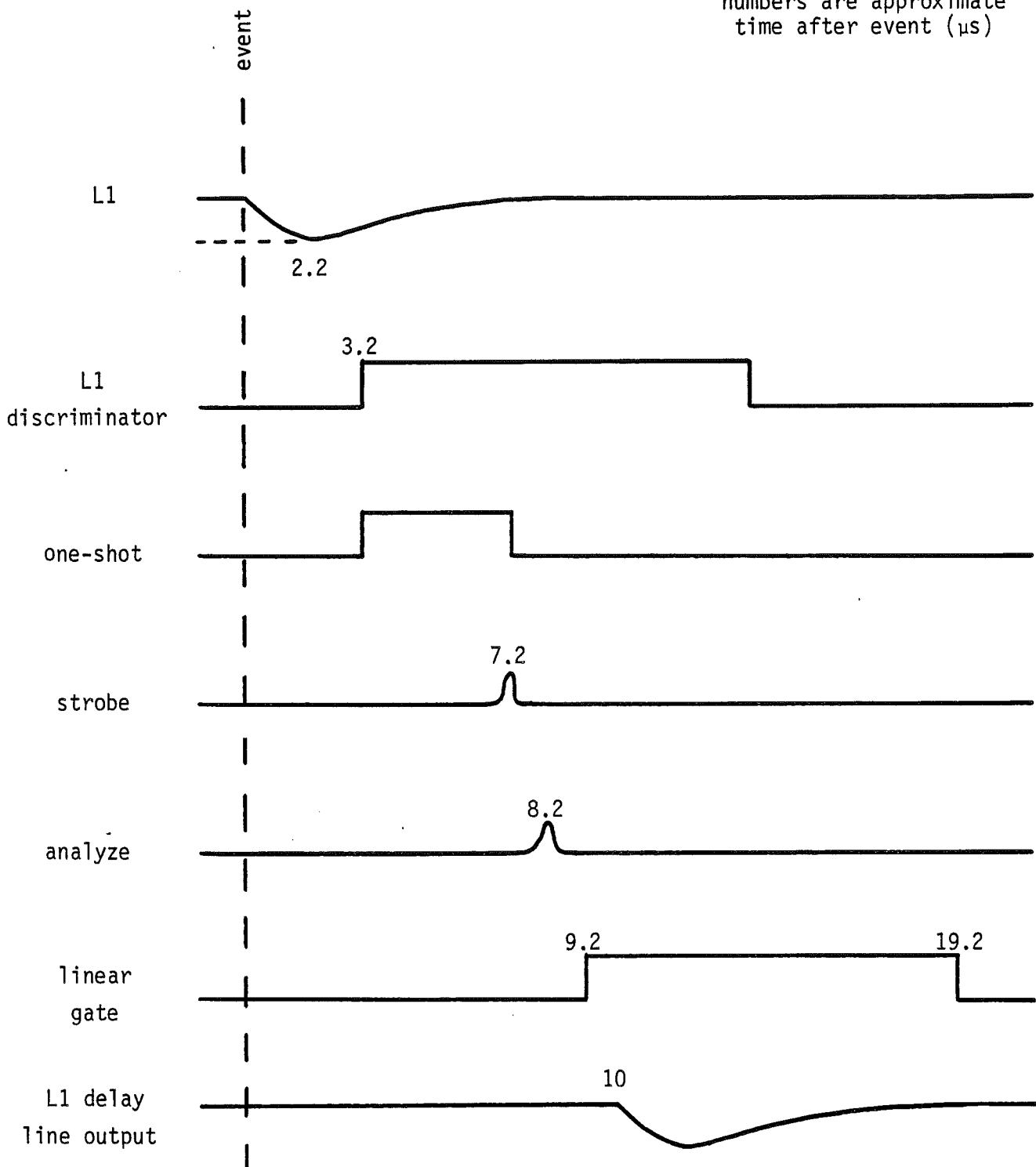


**Figure 4**

Timing diagram for the PHA linear gate. Shown, from top to bottom, are the L1 amplifier output, the L1 discriminator state, the one-shot state, the strobe, the analyze pulse which occurs when coincidence is established, the linear gate (up means open), and the signal at the end of the L1 delay line.

numbers are approximate  
time after event ( $\mu\text{s}$ )



takes a constant current source to discharge the capacitor. This time is proportional to the height of the input pulse, and therefore to the particle energy loss in the detector.

In addition to pulse-height analyzing select events, the CRS instrument also measures several coincidence rates and single discriminator rates. The rates that are measured by the LETs are listed in Table 1. The slant discriminator is triggered whenever  $E1 + 0.42E2 + 0.20E3 > 9.6$  MeV, where  $E1$ ,  $E2$ , and  $E3$  are the energy losses in L1, L2, and L3. The purpose of this discriminator is to distinguish between events with  $Z < 3$  and those with  $Z \geq 3$ . Note that the slant rate (SL rate) is not a coincidence rate, so that, for example, an event with  $E1 > 9.6$  MeV, but no signals in L2 and L3, will be counted. The geometry factor for L1 events (entering through the window) is  $4.6 \text{ cm}^2\text{-sr}$  whereas that for L1·L2 events and L1·L2·L3 events is  $0.44 \text{ cm}^2\text{-sr}$ . Therefore, it is often a good approximation to assume that the SL rate is just that of particles with  $E1 > 9.6$  MeV. Another example demonstrates the pileup characteristics of the SL rate. Consider a particle 1 with  $E1_1 = 4$  MeV and  $E2_1 = 0$  MeV, and a particle 2, incident a time  $t$  later, with  $E1_2 = 4$  MeV and  $E2_2 = 4$  MeV. If  $t = 0$ , the slant discriminator will be triggered, since  $E1_1 + E1_2 + 0.42E2_2 = 9.7 \text{ MeV} > 9.6 \text{ MeV}$ . For  $t > 0$ , the triggering of the discriminator will depend on whether or not the outputs from the L1 and L2 amplifiers ever have a weighted sum greater than 9.6 MeV. The shaping time of the amplifiers is  $2.2 \mu\text{s}$ , so that the triggering requirement for this near-threshold example is  $t < 2 \mu\text{s}$ . Thus, the SL rate will not be contaminated by piled-up small pulses (protons or electrons) until the incident rate of the small pulses greatly exceeds  $\sim 10^8 \text{ s}^{-1}$ .

The LZ3\* and LZ3 rates listed in Table 1 are coincidence rates whose definition depends on the command state of the instrument. In the L1·L2·L3 command state all three detectors are included in the coincidence equation, in

TABLE 1  
LET Rates

Rate	Condition
L1	$E1 > 200 \text{ keV}$
L2	$E2 > 200 \text{ keV}$
L3	$E3 > 1.0 \text{ MeV}$
L4	$E4 > 300 \text{ keV}$
SL (slant)	$E1 + 0.42E2 + 0.20E3 > 9.6 \text{ MeV}$
LTRP (triples)	$L1 \cdot L2 \cdot L3 \cdot L4^* \text{ coincidence}^\dagger$
LZ3*	$L1 \cdot [L2] \cdot [L3] \cdot L4^* \cdot SL^* \text{ coincidence}^\dagger$
LZ3	$L1 \cdot [L2] \cdot [L3] \cdot L4^* \cdot SL \text{ coincidence}$

<sup>†</sup> . means logical and, \* means logical not, [] indicates that the term can be deleted from the coincidence equation on command

the L1-L2 state only L1 and L2 are included, and in the L1 state only L1 is included. Events that trigger the slant discriminator are counted in the LZ3 rate, and those that do not are counted in the LZ3\* rate. These two rates are important in higher rate environments where only a small fraction of the valid coincidence events are pulse-height analyzed, since they can be used to normalize the PHA event rate. For example, if  $n_{\text{pha-oxy}}$  oxygen events and  $n_{\text{pha-tot}}$  total events are pulse-height analyzed in a time  $t$ , and  $n_{\text{rate}}$  events are counted in the LZ3 rate, the total incident rate of oxygen nuclei,  $r_{\text{oxy}}$ , satisfying the specified coincidence requirement is

$$r_{\text{oxy}} = \frac{n_{\text{pha-oxy}}}{n_{\text{pha-tot}}} \frac{n_{\text{rate}}}{t} \quad (1)$$

Equation 1 is only valid if the all events in the LZ3 rate have equal probabilities of being pulse-height analyzed. This condition is assumed to be always true since every valid coincidence counted in the LZ3 rate will open the linear gates to the PHAs if the analyzers are not busy. Note that the coincidence and tag conditions applied to the pulse-height analyzed events in obtaining  $n_{\text{pha-tot}}$  should be identical to those required of the events in  $n_{\text{rate}}$ . In particular, the tag requirements on  $n_{\text{pha-tot}}$  should match the instrument command state. Also, since events with the caution tag are counted by the rate scalars (Don Stilwell, private communication), these events should be included in  $n_{\text{pha-tot}}$ . Equation 1 must be modified slightly if the rate requires livetime corrections, as will be discussed below (equations 6 and 9).

### Standard Livetime Correction Formulas

We now consider the response of both a single discriminator, and of two or more discriminators in coincidence, to high triggering rates. There are three characteristic states of a discriminator as illustrated in Figure 5. The zero state is when the discriminator is available for triggering, the up state is after a trigger when the value of the discriminator output is one, and the dead state is when the discriminator is recovering from a previous trigger and is therefore not available for a new trigger, and yet the output is zero. The length of time a discriminator is up is the up time,  $\tau_{up}$ , the length it is dead is the dead time,  $\tau_{dead}$ , and the shortest time after a trigger before the discriminator can be retriggered is the retrigger time,  $\tau_{retrig}$ . Clearly,  $\tau_{retrig} = \tau_{up} + \tau_{dead}$ . The values for these times depend on the size of the triggering and retriggering pulses, as will be discussed in detail below. For pulse heights in the range channel 20 - 2000 ( $\Delta E \approx 1.5-150$  MeV in L1 and L2),  $\tau_{up}$  and  $\tau_{dead}$  are on the order of  $10 \mu s$ .

During periods of high counting rate, the finite retrigger time of a discriminator can cause a significant fraction of the incident particles to not be counted. If  $R_{true}$  and  $R_{obs}$  are the rates of incident particles and observed particles (i.e. counted by the discriminator) respectively, then the numbers of particles not counted per unit time due to the discriminator being up or dead is  $(\tau_{retrig} \cdot R_{obs}) \cdot R_{true}$ . We therefore find that

$$R_{true} = R_{obs} + \tau_{retrig} R_{obs} R_{true}$$

or

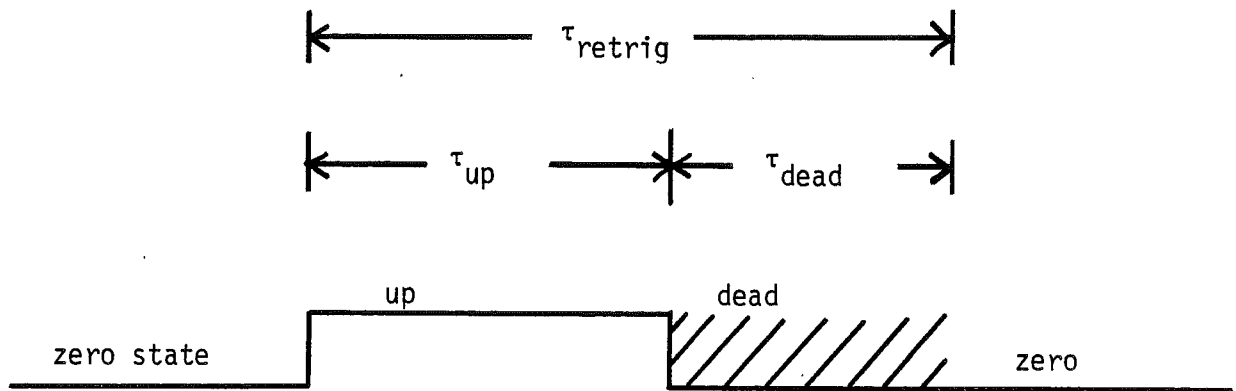
$$R_{true} = \frac{R_{obs}}{(1 - \tau_{retrig} R_{obs})} \quad (2)$$

Using equation 2 one can calculate the true rate, given an observed rate and a



**Figure 5**

Characteristic states of a discriminator.



value for  $\tau_{\text{retrig}}$ . The factor  $1/(1 - \tau_{\text{retrig}}R_{\text{obs}})$  is called the livetime correction factor. The decrease in  $R_{\text{obs}}/R_{\text{true}}$  toward higher counting rates is often referred to as a "deadtime effect", which should not be confused with the more restricted definition of "dead time" shown in Figure 5.

Turning now to the case of a coincidence rate, we show in Figure 6 the L1, L2, L3, and slant discriminator outputs for a typical  $Z \geq 3$ , three-detector event. The discriminators are shown to start their up state at slightly different times and are shown to have different values for  $\tau_{\text{up}}$  and  $\tau_{\text{dead}}$  as would occur in the general case. In order to determine the livetime correction formula corresponding to equation 2 for a coincidence rate, it is necessary to know or estimate the degree of correlation of the various discriminators. For instance, if the singles rates of the detectors are low it will be a good assumption that there will be an L1 trigger for each L2 or L3 trigger (neglecting the slant for now and assuming the spectrum is such that most particles enter through the window). In this case, if one makes the further assumption that the L1 retrigger time is greater than or equal to the L2, L3, and slant retrigger times, then the true coincidence rate,  $C_{\text{true}}$ , will be related to the observed coincidence rate,  $C_{\text{obs}}$ , by

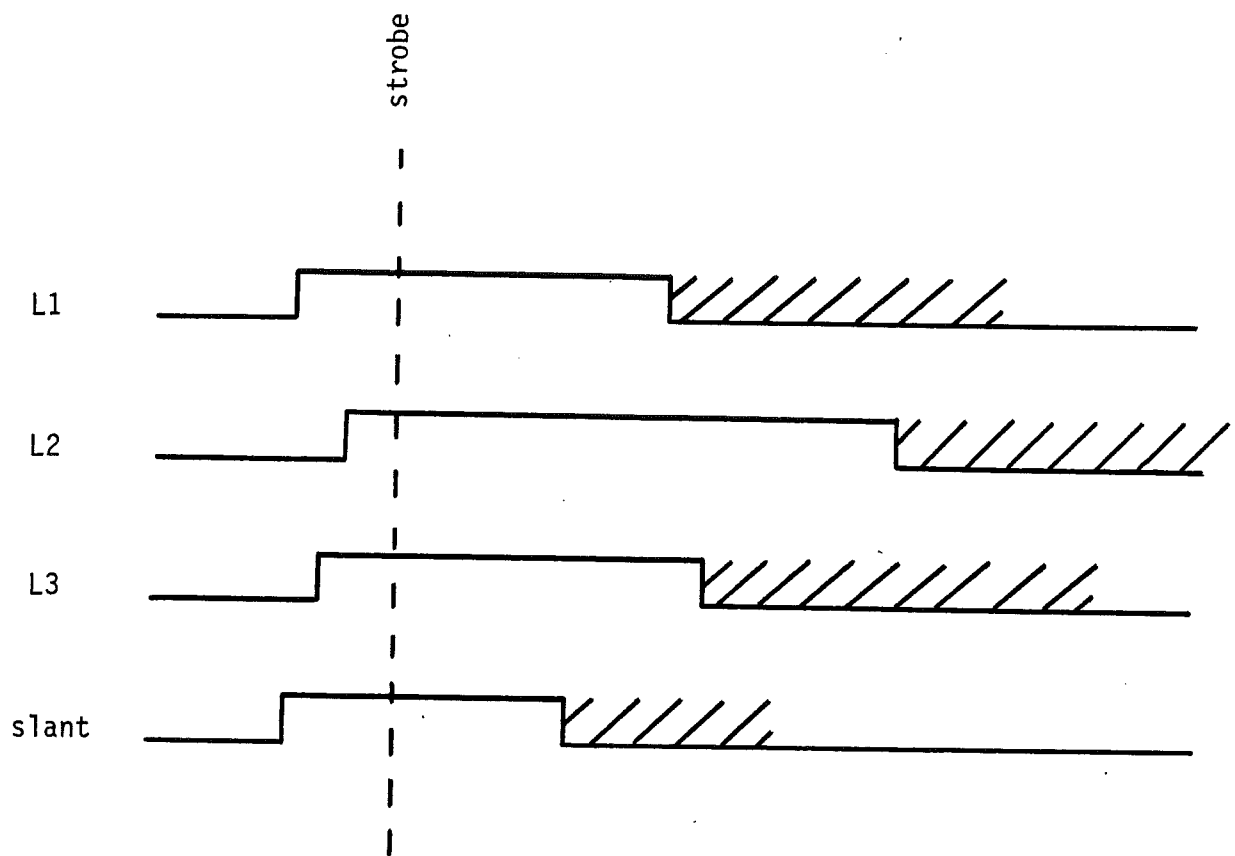
$$C_{\text{true}} = \frac{C_{\text{obs}}}{(1 - \tau_{1 \text{ retrig}} R_1)} \quad (\text{low flux}) \quad (3)$$

where  $\tau_{1 \text{ retrig}}$  and  $R_1$  are the L1 retrigger time and singles rate respectively. In the other extreme, if the singles rates of the detectors are high, it will be a good assumption that the discriminators are being triggered independently of one another. In this case there will be a livetime correction factor,  $1/(1 - \tau R)$ , for each detector, so that for three-detector events,

$$C_{\text{true}} = \frac{C_{\text{obs}}}{(1 - \tau_{1 \text{ retrig}} R_1)(1 - \tau_{2 \text{ retrig}} R_2)(1 - \tau_{3 \text{ retrig}} R_3)} \quad (\text{high flux}) \quad (4)$$

**Figure 6**

Typical L1, L2, L3, and slant discriminator outputs for a three-detector event.



For certain types of analysis, an added complication having to do with event recognition requires equations 3 and 4 to be modified. In the above discussion it is assumed that the only way an event can be counted in  $C_{obs}$  is if it triggers all three detectors itself. However, if, for example, the most common event type is protons (i.e. small pulses), and the objective is to determine the livetime correction for the LZ3 rate, it will be possible for some  $Z \geq 3$  events to be counted in the LZ3 rate even if they do not trigger every discriminator themselves. Two examples are shown in Figure 7. In Figure 7a a small pulse triggers L1, but not L2, L3, or the slant, and  $\sim 4 \mu s$  later the strobe occurs. If there were no other event, the established coincidence at the time of the strobe would not match any coincidence requirement (assuming the instrument was not in the L1 command state) and the event would not be counted in a coincidence rate and would not be pulse-height analyzed. However, in the time between the proton event and the strobe a three-detector  $Z \geq 3$  event occurs, triggering the L2, L3, and slant discriminators in time for the strobe to see them. The  $Z \geq 3$  event therefore is counted in the LZ3 rate and is pulse-height analyzed. The L2 and L3 pulse heights will be nominal while that of L1 will be shifted upward by the proton pulse. For an oxygen nucleus just stopping in L3 and a proton just stopping in L1 (i.e. minimum  $E1_{oxygen}$  and maximum  $E1_{proton}$ ),  $E1$  will be shifted upward from the nominal oxygen track by  $\sim 14\%$ , while the  $E1$  separation between the nominal oxygen and fluorine tracks at constant  $E2+E3$  is  $\sim 26\%$ . Hence, the oxygen event will still be recognizable. Therefore, for the case of an L1 rate dominated by small pulses, the L1 livetime correction factor for the LZ3 rate should be  $1/[1 - (\tau_{1\text{retrig}} - \tau_{\text{strobe}})R_1]$  in equations 3 and 4, since there is an additional livetime of approximately  $\tau_{\text{strobe}}$  per L1 trigger.

In Figure 7b, attention is focused on the L2 discriminator. In all three small figures ( $b_1, b_2, b_3$ ), the L1 and slant discriminators are triggered by a  $Z \geq 3$

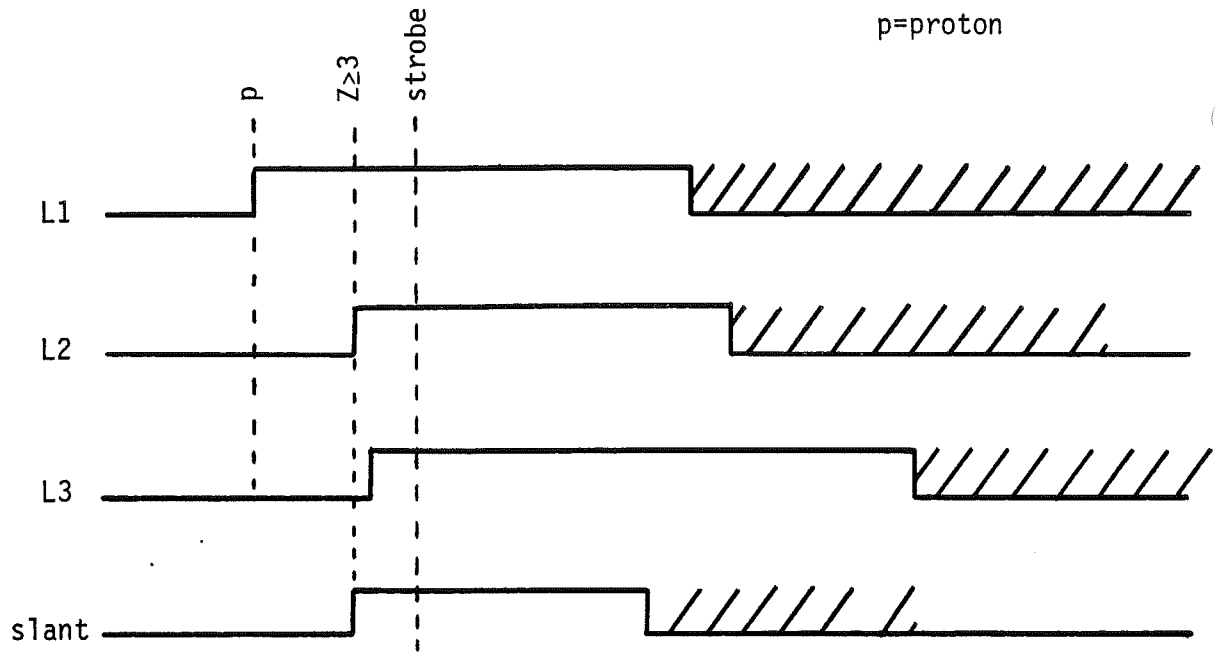
**Figure 7**

Discriminator timing diagrams for a proton and  $Z \geq 3$  event in near coincidence.

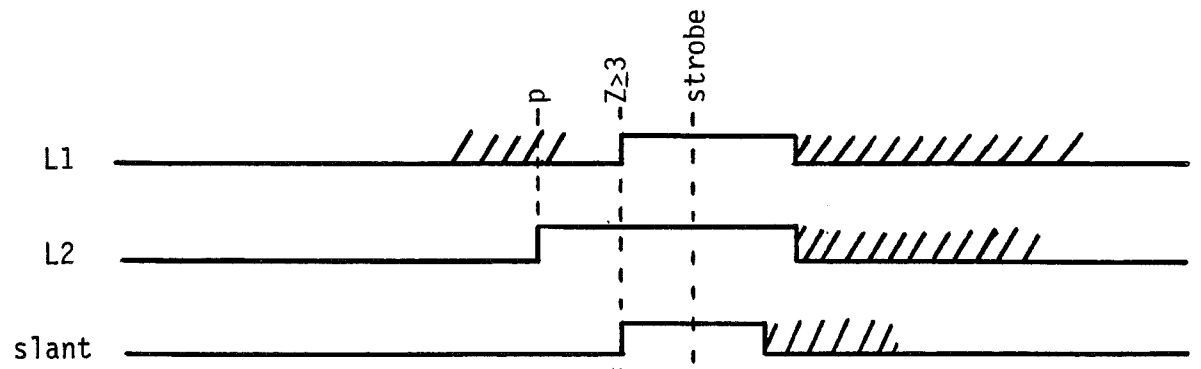
- a) The proton causes the strobe.
- b) Three cases where the  $Z \geq 3$  event causes the strobe. For simplification, L3 is not shown.

p=proton

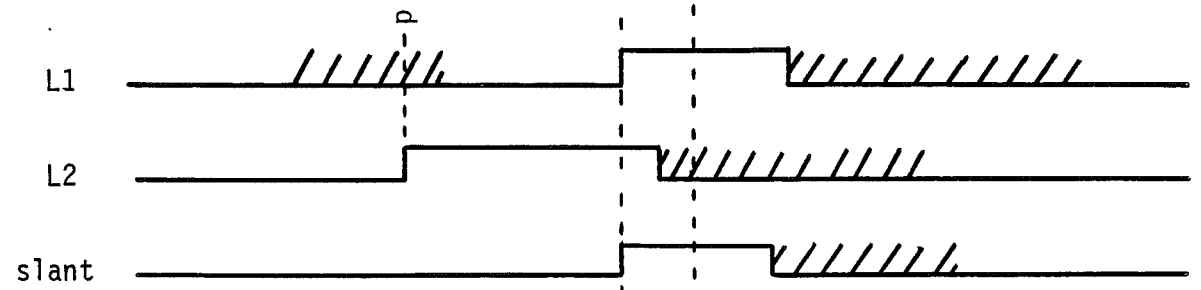
a)



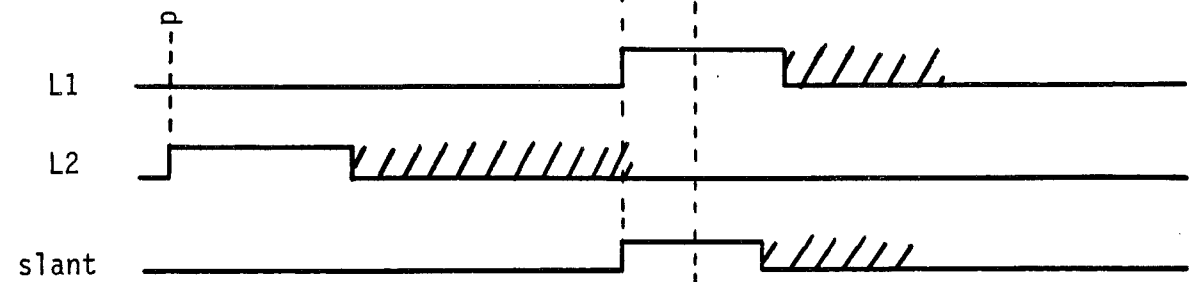
b<sub>1</sub>)



b<sub>2</sub>)



b<sub>3</sub>)





event, and the L2 discriminator by a proton that precedes the  $Z \geq 3$  event. In Figure 7b<sub>1</sub>, the strobe (caused by the  $Z \geq 3$  event) comes when the L2 discriminator is up, and the event is therefore counted in the LZ3 rate and is pulse-height analyzed. As in the L1 example, the L2 pulse height is shifted upward by the proton pulse. In Figure 7b<sub>2</sub>, the strobe comes when the L2 discriminator is dead and consequently there is no rate count or pulse-height analysis. In Figure 7b<sub>3</sub>, the L2 discriminator is dead at the time of the  $Z \geq 3$  event and down at the time of the strobe, so that again analysis does not occur. This example shows that  $\tau_{2 \text{ retri}}$  should be replaced by  $\tau_{2 \text{ dead}} + \tau_{\text{strobe}}$  in equation 4. A similar change occurs for L3, so that, including all effects, equation 4 becomes

$$C_{\text{true}} = \frac{C_{\text{obs}}}{[1 - (\tau_{1 \text{ retri}} - \tau_{\text{strobe}})R_1][1 - (\tau_{2 \text{ dead}} + \tau_{\text{strobe}})R_2][1 - (\tau_{3 \text{ dead}} + \tau_{\text{strobe}})R_3]} \quad (5)$$

Since  $C_{\text{true}}$  is the true rate of incident particles satisfying the coincidence condition, it is the rate that should be used in equation 1 to normalize the pulse-height analyzed events. For events of type  $i$

$$r_i = \frac{n_{\text{pha}-i}}{n_{\text{pha-tot}}} C_{\text{true}} = \frac{n_{\text{pha}-i}}{n_{\text{pha-tot}}} \lambda C_{\text{obs}} \quad (6)$$

where  $\lambda$  is the livetime correction factor, assumed independent of event type. However, as will be discussed in later sections, the livetime correction factors used in calculating  $C_{\text{true}}$  actually do depend on the event type. Therefore, if  $C_{\text{obs}-i}$  is the observed rate and  $\lambda_i$  is the livetime correction factor for events of type  $i$  ( $C_{\text{true}-i} = \lambda_i C_{\text{obs}-i}$ ), the true coincidence rate that would be observed with a perfect 100% live instrument is  $C_{\text{true}} = \sum_i \lambda_i C_{\text{obs}-i}$ . (For the LZ3 rate,  $i$  runs from lithium to nickle.) The question is, what is the correct expression to replace equation 6 for the case of different  $\lambda_i$ ? Since a constant fraction,  $\epsilon$ , of

all observed rate counts are pulse-height analyzed, the number of events of type  $i$  that are pulse-height analyzed in a time  $t$  is

$$n_{\text{pha}-i} = t \varepsilon C_{\text{obs}-i} = t \varepsilon \frac{C_{\text{true}-i}}{\lambda_i} . \quad (7)$$

Therefore, the total number of events that are pulse-height analyzed in time  $t$  is

$$n_{\text{pha-tot}} = t \varepsilon \sum_i C_{\text{obs}-i} = t \varepsilon C_{\text{obs}} . \quad (8)$$

Combining equations 7 and 8 gives the correct generalization of equation 6:

$$r_i = C_{\text{true}-i} = \frac{n_{\text{pha}-i}}{n_{\text{pha-tot}}} \lambda_i C_{\text{obs}} . \quad (9)$$

Note that  $C_{\text{true}}$  does not appear. This is good because one would have to know the livetime correction factors for all event types in order to calculate  $C_{\text{true}}$ . The quantity  $\lambda_i C_{\text{obs}}$  that does appear in the equation has no physical meaning since  $C_{\text{obs}}$  is a mixture of all event types whereas  $\lambda_i$  is the livetime correction factor for event type  $i$  only.

### Calibration Descriptions

As mentioned in the previous section, the characteristic discriminator times, and therefore the livetime correction factors for events of interest, depend on the signal size and frequency of both the events of interest and the majority events that are triggering the discriminator. Thus, in order to obtain accurate fluxes from the rate measurements made in high radiation environments, it is necessary to measure the  $\tau$ 's, or ideally the livetime correction factors themselves for the specific conditions that were encountered. Following the Voyager 1 and 2 encounters with Jupiter in March and July of 1979 (Vogt *et al.*, 1979a,b), there was particular interest in determining the LZ3 and SL livetime corrections for oxygen and sulfur nuclei in the presence of large fluxes of protons and electrons. In 1979 and 1980 three separate calibrations were performed using the spare CRS instrument. The first was organized and carried out by J. H. Trainor, D. E. Stilwell, and M. F. Beazley at the Goddard Space Flight Center during the time of the encounters. Detector signals were simulated by pulse generators connected to the amplifier inputs, and pulses were put into various combinations of amplifiers, usually in pairs. By varying the time between pulses and the pulse size, a wide range of characteristic discriminator times was measured.

The second and third calibrations were organized and carried out by E. C. Stone, myself, M. F. Beazley, and R. Burrell. For these runs, the ionization energy loss of charged particles in the detectors was simulated by pulsing light emitting diodes (LEDs) situated above the detectors. As far as the detector amplifiers and electronics are concerned, the detector output is the same for ionization created by incident photons as that created by penetrating charged particles, provided the light pulse is short compared to the amplifier shaping

time. During the calibrations, the light pulses were always shorter than 100 ns and were therefore very much shorter than the  $2.2 \mu\text{s}$  amplifier shaping times. The advantage of using LEDs is that no direct inputs into the detector-amplifier-discriminator circuit are required, so that the circuit response is unchanged from the flight configuration. Also, several different particle species and rates in a single detector can be easily simulated by placing several LEDs above it and pulsing them simultaneously and independently at different rates and intensities. The LEDs were pulsed by fast square-wave pulse generators triggered by random pulse generators (second calibration) or radioactive sources (third calibration). The setup and other details of the LED calibrations are given in the Appendix.

### Calibration Results

In this section several results from the three calibrations will be presented. The emphasis will be on results that are needed to obtain absolute fluxes of oxygen and sulfur nuclei in the presence of high proton and electron fluxes. The two subsections deal with livetime corrections for the SL and L1 singles rates and the LZ3 coincidence rate respectively. Discriminator times were in general measured both with the pulser and the LED techniques, with excellent agreement obtained between them. Direct measurements of the livetime correction factors (or equivalently  $R_{\text{true}}$  as a function of  $R_{\text{obs}}$ ) were made only with the LED technique. In both subsections, wherever possible, the variation in the results between the four different LETs (LET A, B, C, and D) will be given. This is important because the measurements made with the spare CRS instrument are to be applied to the two flight units. The variation between LETs in a

given instrument should be a good indication of the uncertainty involved in extrapolating the results to the other units.

### SL and L1 Singles Rates

During the second and third calibrations, measurements were made of the observed vs true SL and L1 rates for several different sized input pulses. The measurement technique was simply to input a known random rate <sup>†</sup> of pulses of a given size into the L1 detector and record the SL or L1 rate returned from the instrument. The observed SL rate,  $SL_{obs}$ , is shown as a function of the true input rate,  $SL_{true}$ , in Figure 8 for both 30 and 90 MeV pulses in L1 (channels 400 and 1200). These results, as well as those for 15 MeV pulses are listed in Table 2. The reason that 15, 30, and 90 MeV pulses were chosen is that peaks were seen (Gehrels *et al.*, 1981) in the L1 pulse-height distribution (slant required) at these energies in different regions of the Jovian magnetosphere. The 30 and 90 MeV peaks were interpreted respectively as being to ~5 MeV/nuc oxygen and sulfur ions penetrating L1, while the 15 MeV peak was likely due to a pulse-height distribution increasing toward smaller pulses and cut off by the 9.6 MeV slant threshold. Also shown in Figure 8 are lines of constant  $\tau_{retrig}$  in equation 2 for  $\tau_{retrig} = 10, 20, \text{ and } 30 \mu s$ . The 30 MeV data are seen to be well represented up to  $SL_{true} \approx 7 \times 10^4 \text{ s}^{-1}$  by a constant  $\tau_{retrig}$  of between 15 and 20  $\mu s$ . The 90 MeV data have an effective  $\tau_{retrig}$  that increases from 20 to 30  $\mu s$  toward higher rates, demonstrating that a constant  $\tau_{retrig}$  is not a good model for the discriminator response to pulses of this size. For comparison, double-pulse measurements of the slant retrigger times are listed in Table 3 for various pulse size combinations. The retrigger time for 30 MeV double pulses is 17.5  $\mu s$ , which is

<sup>†</sup> "Random rate" means that the pulses are random in time with some constant average rate.

**Figure 8**

Measurements of the observed SL rate as a function of the true input rate of 30 and 90 MeV pulses. The data are also listed in Table 2. The dashed lines are lines of constant  $\tau_{\text{retrig}}$  in equation 2, i.e.,  $SL_{\text{true}} = SL_{\text{obs}} / (1 - \tau SL_{\text{obs}})$ .

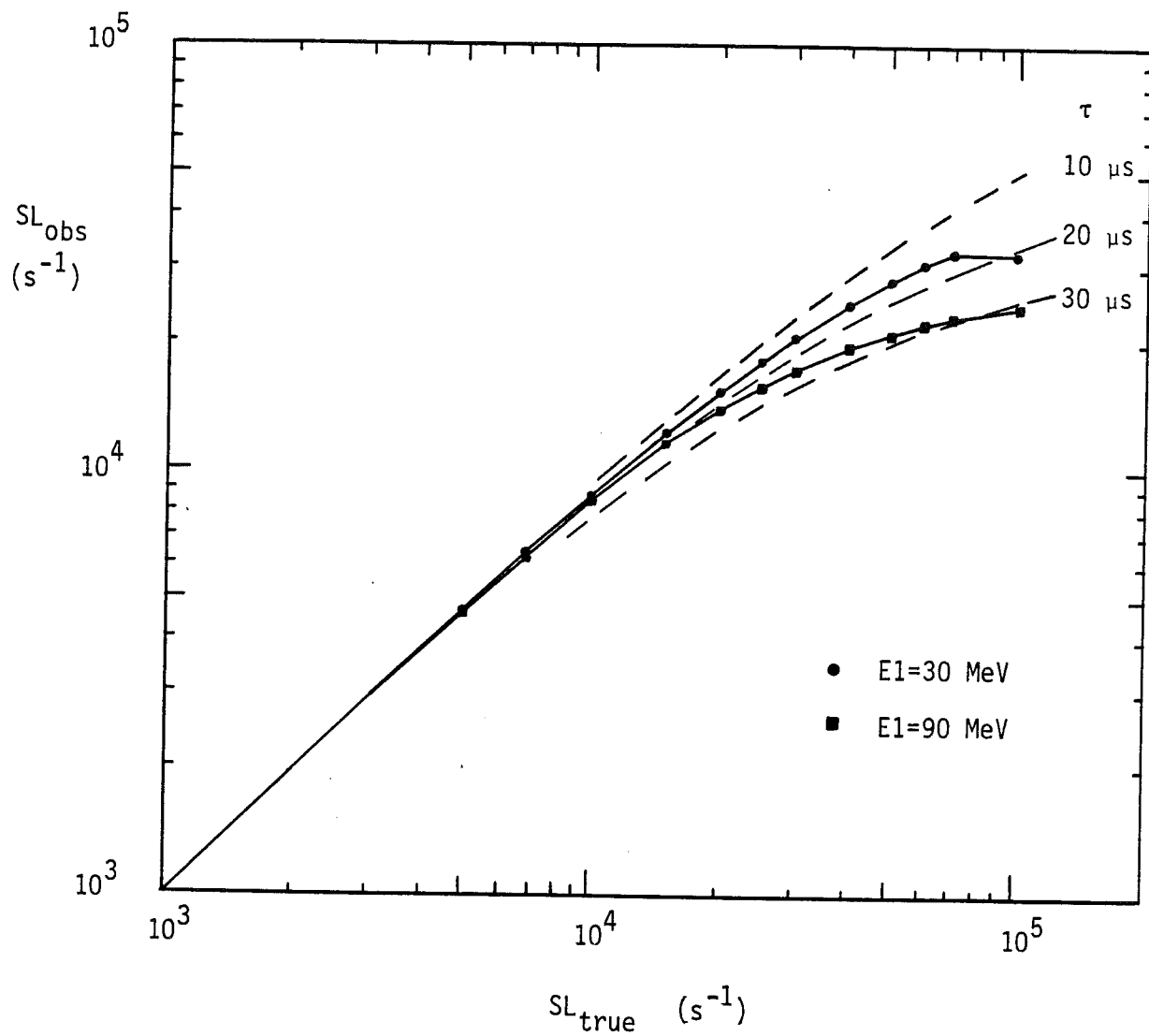


TABLE 2

Observed vs True Slant Rate<sup>†</sup>  
for Several L1 Pulse Heights<sup>†</sup>

SL <sub>true</sub> (10 <sup>3</sup> s <sup>-1</sup> )	SL <sub>obs</sub>		
	E1=15 MeV (10 <sup>3</sup> s <sup>-1</sup> )	E1=30 MeV <sup>*</sup> (10 <sup>3</sup> s <sup>-1</sup> )	E1=90 MeV <sup>*</sup> (10 <sup>3</sup> s <sup>-1</sup> )
5	4.7	4.7	4.7
7	6.5	6.5	6.3
10	8.9	8.8±0.2 <sup>††</sup>	8.6
15	12.6	12.3	11.6
20	15.9	15.5	14.0
25	18.8	18.3	15.8
30	20.3	21.0	17.5
40	20.5	24.9	19.5
50	18.5	28.2±1.5	21.1
60	17.6	30.7	22.3
70	17.5	32.9	23.2
80	18.8	-	-
90	20.2	-	-
100	21.4	32.5±2.5	24.5

<sup>†</sup> E2=0, E3=0

<sup>\*</sup> Plotted in Figure 8.

<sup>††</sup> The indicated errors are typical standard deviations of the measured SL<sub>obs</sub> in LET A, B, C, and D.



TABLE 3  
Slant Discriminator Retrigger Times<sup>†</sup>

		A pulse height* (E1 in MeV)				
		15	30	90	120	240
B pulse height* (E1 in MeV)	15	16.2 $\mu$ s	16.9	-	18.5	18.8
	30	16.8	17.5	-	19.8	20.5
	90	-	-	19.5	-	-
	120	17.1	17.9	-	20.0	20.8
	240	17.5	18.3	-	20.2	21.0

<sup>†</sup> The standard deviation of the retrigger time measured in LET A, B, C, and D is typically 0.3  $\mu$ s.

\* The values listed are the minimum time between pulses A and B for which both pulses are counted by the slant discriminator.

in reasonable agreement with the effective retrigger time deduced from the 30 MeV data in Figure 8.

Looking at the 15 MeV data in Table 2, one sees that for  $SL_{true} < 3 \times 10^4 \text{ s}^{-1}$ , the observed SL rate at a given true rate is approximately the same as that of the 30 MeV pulses. However, between true rates of  $4 \times 10^4$  and  $7 \times 10^4 \text{ s}^{-1}$ , the observed rate for the 15 MeV pulses actually decreases slightly toward increasing true rate! This rollover in the observed vs true rate also occurs for various sized pulses in other LET discriminators as we shall see for L1, and is not uncommon in discriminator circuits in other particle instruments (J. H. Trainor, private communication). During the calibrations it was observed that an inverted response of this type can also occur when large pulses are added to a small-pulse dominated discriminator. This effect will be discussed in the last section of the report.

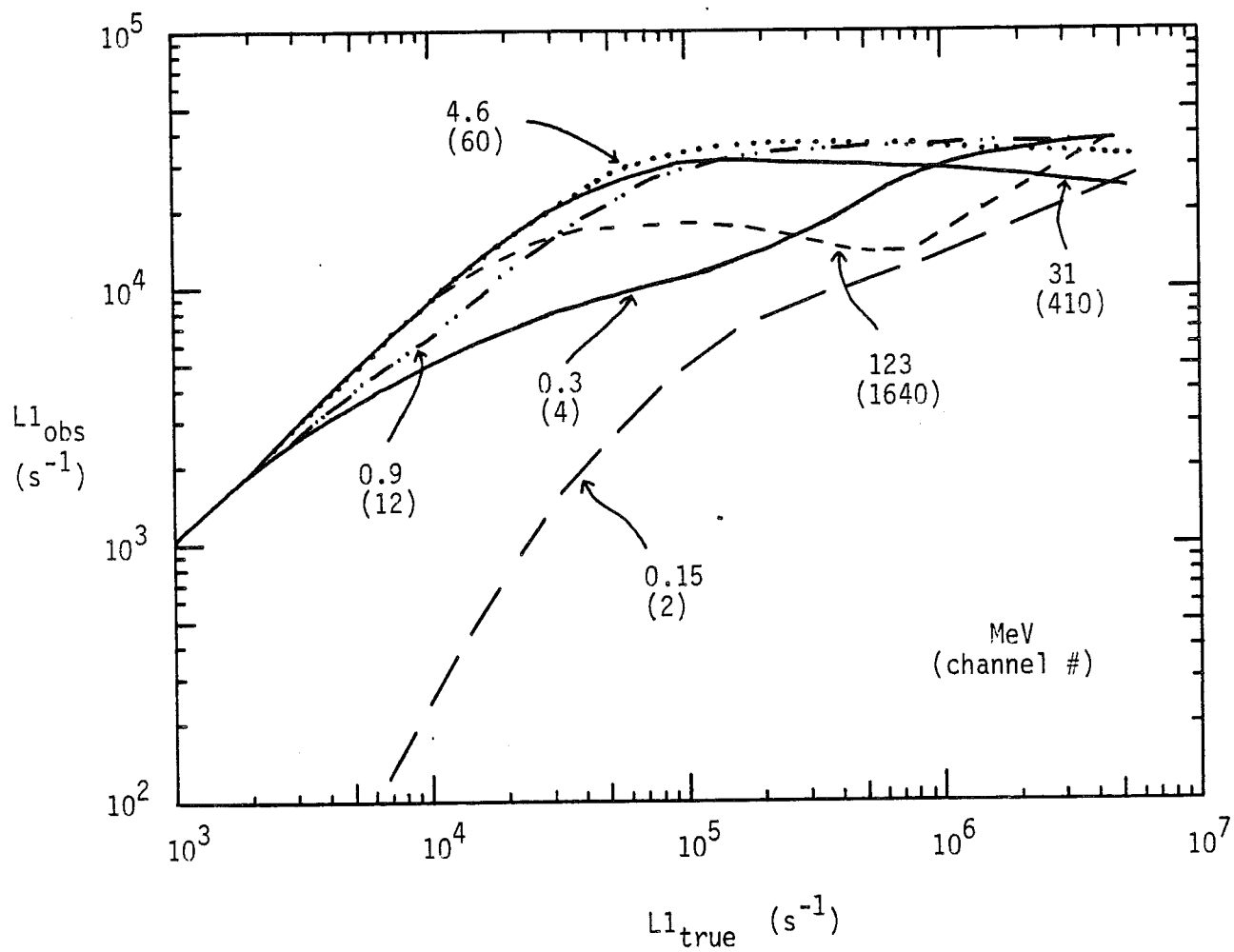
The observed L1 rate,  $L1_{obs}$ , is shown as a function of the true input rate,  $L1_{true}$ , in Figure 9 for six different pulse sizes between 0.15 MeV and 123 MeV (L1 discriminator threshold = 0.2 MeV, full scale  $\approx 300$  MeV). Since the 0.15 MeV pulses are below threshold it is not surprising that, at low rates, few are counted. In fact, at rates where livetime effects are unimportant, one can estimate how many events are expected. We assume that two 0.15 MeV pulses must occur within the  $\sim 2 \mu\text{s}$  shaping time of the amplifier in order to trigger the discriminator. Then, for a given true rate, the expected observed rate is

$$L1_{obs} = L1_{true} (1 - e^{-L1_{true} \cdot 2\mu\text{s}}) \quad (10)$$

(see, e.g., Evans, 1955, p.754). For example, if  $L1_{true} = 10^4 \text{ s}^{-1}$ , one expects  $L1_{obs} = 200 \text{ s}^{-1}$ , which is quite close to the value actually measured. Toward higher rates, the measured  $L1_{obs}$  for 0.15 MeV pulses is less than equation 10 predicts, due to deadtime effects.

**Figure 9**

The observed L1 rate as a function of the true input rate for several pulse sizes. The channel numbers indicated are not the numbers returned by the instrument PHAs, but were calculated from the pulse sizes at the amplifier output (measured with an oscilloscope) assuming a linear conversion.



The maximum  $L1_{obs}$  in Figure 9, for several pulse sizes, is  $\sim 4 \times 10^4 \text{ s}^{-1}$  which correlates well with the fact that all L1, L2, and L3 singles rates saturated near this value during the Voyager 1 and 2 closest approaches to Jupiter. A maximum rate of  $\sim 4 \times 10^4 \text{ s}^{-1}$  corresponds to an effective retrigger time of  $25 \mu\text{s}$ . For comparison and for general reference, the measured L1 discriminator retrigger times are listed in Table 4. The table shows that  $25 \mu\text{s}$  is not an unreasonable retrigger time. Finally, as in the case of 15 MeV pulses for the SL rate, the 31 and 123 MeV curves in Figure 9 both have regions where the observed L1 rate decreases toward higher true rates.

#### LZ3 Coincidence Rate

As shown in the livetime formulas section, the true incident rate,  $r_i$ , of a given event type,  $i$ , can be calculated using equation 9:  $r_i = (n_{pha-i} / n_{pha-tot}) \lambda_i C_{obs}$ . Since  $n_{pha-i}$ ,  $n_{pha-tot}$ , and  $C_{obs}$  are all measured quantities, the objective here is to determine  $\lambda_i$  (the livetime correction factor for coincidence rate  $C_{obs}$  for event type  $i$ ). In general,  $\lambda_i$  can be separated into terms for each detector required in the coincidence, so that, for instance for three-detector events,

$$\lambda_i = \lambda_{1i} \cdot \lambda_{2i} \cdot \lambda_{3i} \quad (11)$$

For the case of heavy nuclei in the presence of large fluxes of protons and electrons, the separate terms can be expressed as functions of the effective discriminator times,

$$\lambda_{1i} = \frac{1}{[1 - (\tau_{(1 \text{ retrigger})-i} - \tau_{\text{strobe}})R_1]} \quad (12a)$$

$$\lambda_{xi} = \frac{1}{[1 - (\tau_{(x \text{ dead})-i} + \tau_{\text{strobe}})R_x]} \quad (x=2,3) \quad (b)$$

TABLE 4  
L1, L2, and L3 Discriminator Retrigger Times\*

		<u>L1 and L2</u>						
		A pulse height (channel # <sup>†</sup> )						
		4.1	8.2	20	60	205	410	820
B pulse height (channel # <sup>†</sup> )	3.3	108 $\mu$ s	107	78	53	59	70	71
	4.1	90	84	57	38	45	50	56
	8.2	51	49	27	23	30	33	45
	20	33	32	20	13	18	22	30
	60	34	32	19	14	16	17	18
	410	34	32	20	14	16	18	19
	820	34	32	20	14	16	18	19

A= 12, B= 400 .  $\tau=31 \mu$ s

A=3300, B=3300  $\tau=21 \mu$ s

		<u>L3</u>						
		A pulse height (channel # <sup>†</sup> )						
		4.1	8.2	20	60	205	410	820
B pulse height (channel # <sup>†</sup> )	3.3	90 $\mu$ s	89	41	39	49	58	71
	4.1	77	76	31	32	39	45	66
	8.2	35	34	17	22	27	31	49
	20	36	35	14	13	18	21	29
	410	36	35	15	14	17	18	19

\* Typical variations between L1 and L2 in a given telescope and between the L1s and L2s in different telescopes is 5%. The typical variation in L3 between different telescopes is also 5%.

<sup>†</sup> Channel # is used instead of energy loss to facilitate comparison of L1-L2 and L3 values. The channel numbers use here are defined by

$$(\text{Channel \#})_{L1-L2} = \Delta E_{L1-L2} / 75 \text{ keV} \quad (\text{Channel \#})_{L3} = \Delta E_{L3} / 500 \text{ keV}.$$

(see equation 5). During the calibrations  $\lambda_1$ ,  $\lambda_2$ , and  $\lambda_3$  were directly measured as functions of detector singles rate (small pulses) for both oxygen and sulfur nuclei. In this subsection, the measurements will be presented and compared to equations 12.

The measurement of  $\lambda_1$  for a given L1 singles rate was performed by pulsing L1 with that rate of proton-sized pulses (0.9 MeV), while at the same time pulsing L1 and L2 in coincidence at a low rate ( $\sim 100\text{s}^{-1}$ ) with a large pulse in L1 and 1.8 MeV pulse in L2. The pulse height of the large pulse in L1 was chosen to be typical of either oxygen (30 MeV) or sulfur (90 MeV). The value of  $\lambda_1$  was determined from the fraction of coincidence events that were counted in the LZ3 rate (L1:L2 command state). In Figure 10a measurements of  $\lambda_1$  for oxygen are plotted as a function of the observed L1 singles rate of the small pulses,  $R_1$ , together with a second-order polynomial fit. For comparison, two lines of constant  $\tau_{1\text{ retrigger}} - \tau_{\text{strobe}}$  in equation 12a are shown. The value for  $\tau_{1\text{ retrigger}} - \tau_{\text{strobe}}$  that one would deduce from Table 4 (A pulse = 0.9 MeV = channel 12, B pulse = 30 MeV = channel 400,  $\tau_{\text{strobe}} = 4\text{ }\mu\text{s}$ ) is  $\sim 27\text{ }\mu\text{s}$ . At low rates, the measurements in Figure 10 indicate an effective time that is close to this value. At higher rates, however, the measurements indicate a decreasing effective  $\tau_{\text{retrigger}} - \tau_{\text{strobe}}$  that approaches  $10\text{ }\mu\text{s}$ . This result in particular demonstrates the importance of directly measuring the livetime correction factors for conditions of interest. Although the goal of the calibrations was to make livetime corrections good to only  $\sim 20\%$ , it is clear that assuming a constant retrigger time of, say,  $25\text{ }\mu\text{s}$  would lead to livetime corrections of more than a factor of two too large from L1 alone!

Figure 10b shows the  $\lambda_1$  dependence on event type and telescope. The data in Figure 10a were obtained using LET C. In Figure 10b, the best fit curve for those data is compared to that obtained for LET A. The error bars at the end of

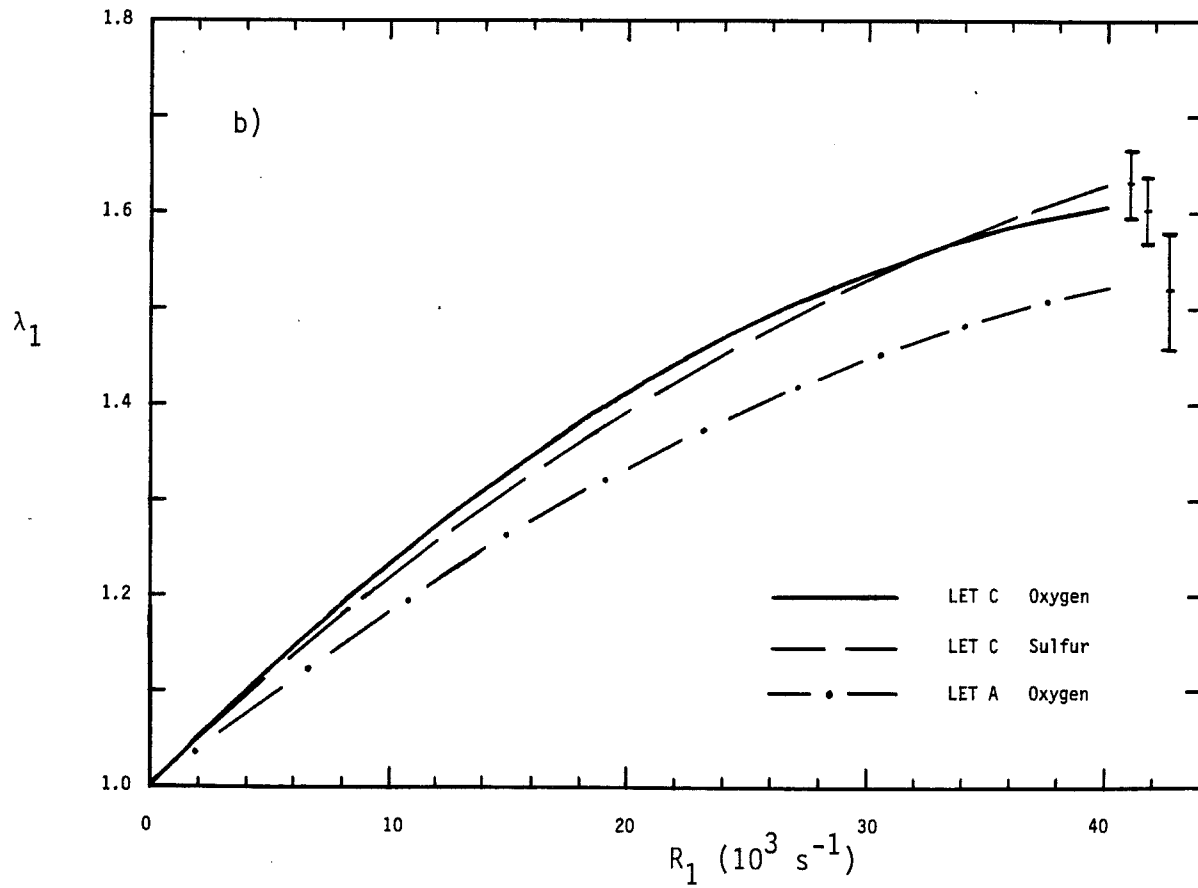
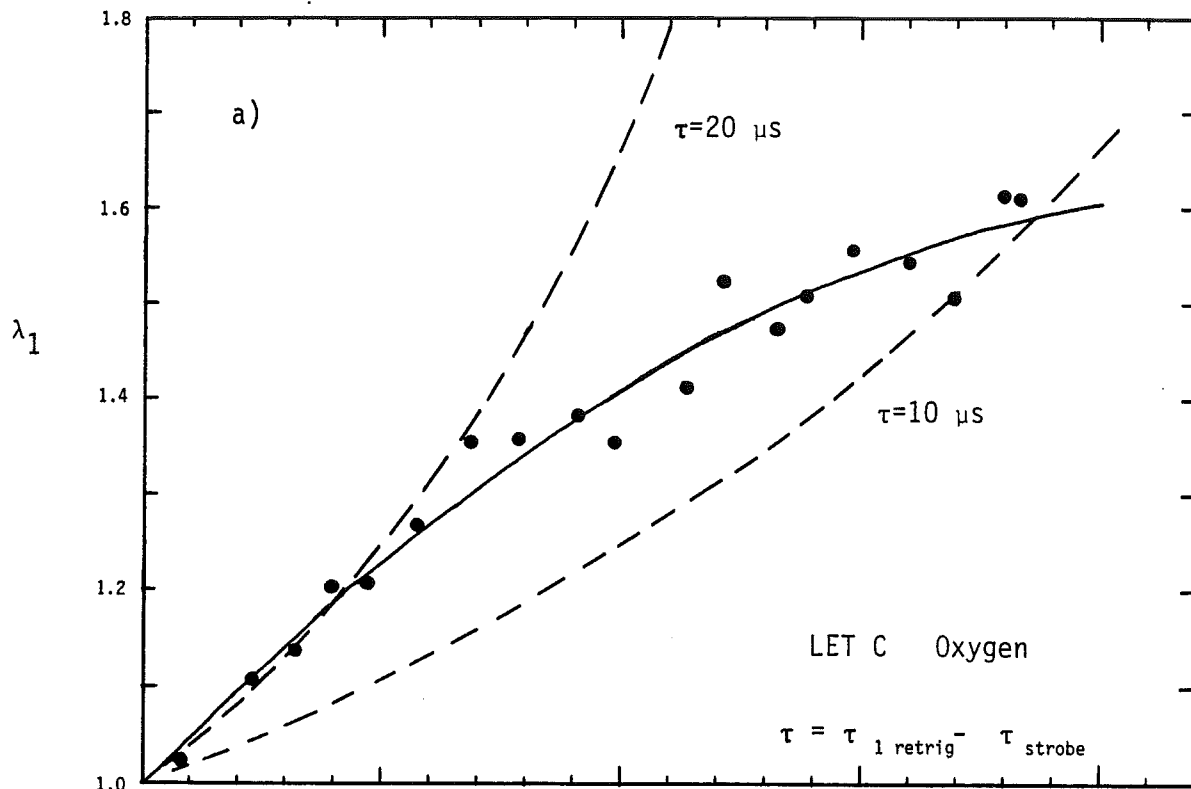
**Figure 10**

Measurements of the L1 livetime correction factor,  $\lambda_1$ , for oxygen and sulfur nuclei, as a function of the L1 singles rate of 0.9 MeV pulses (protons).

a) Oxygen measurements made with LET C. The solid line is a second-order polynomial least-squares fit to the data. The dashed lines are lines of constant  $\tau_{\text{retrig}} - \tau_{\text{strobe}}$  in equation 12a, i.e.,  $\lambda_1 = 1 / (1 - \tau R_1)$  where  $\tau = \tau_{\text{retrig}} - \tau_{\text{strobe}}$ .

b) Oxygen measurements made with LET A and C, and sulfur measurements made with LET C.





each curve represent the approximate spread in the data about the curve. These two curves show that  $\sim 10\%$  variations in  $\lambda_1$  from telescope to telescope can not be ruled out, although the difference between the curves may be mostly due to the uncertainties in the curves. Also shown is the  $\lambda_1$  curve for sulfur obtained using LET C. There is quite good agreement between this result and that obtained for oxygen using LET C, indicating that  $\lambda_1$  does not depend strongly on event type between oxygen (30 MeV) and sulfur (90 MeV).

Before direct measurements of  $\lambda_2$  and  $\lambda_3$  are presented, estimates of their magnitude and rate dependence will be made using the  $\lambda_1$  data. Figure 11 shows the effective retrigger time as a function of rate calculated using equation 12a and the LC1 oxygen measurements of  $\lambda_1$  with  $\tau_{\text{strobe}} = 4 \mu\text{s}$ . It is assumed that this also represents the average retrigger time for L2. Also shown in the figure are measurements of the average L2 discriminator up time. These data were obtained by pulsing L2 with proton-sized pulses (0.9 MeV) at a rate  $R_{\text{obs}}$ , and simultaneously and independently pulsing L1 at a low rate. The ratio of the number of accidental coincidences to the number of L1 pulses represents the fraction of time that the L2 discriminator was up, which, when divided by  $R_{\text{obs}}$ , gives the average up time per counted event in L2. Since  $\tau_{\text{retrig}} = \tau_{\text{dead}} + \tau_{\text{up}}$ , the difference in the curves is a measure of the average dead time. The dead time for this case of a large pulse following a small pulse is seen to be quite small compared to the up time and approaches zero toward lower rates. The implication is that a large pulse can trigger a discriminator almost immediately after it goes down. This estimate of  $\tau_{\text{dead}}$  can now be used with equation 12b to predict  $\lambda_2$  as a function of  $R_2$ . The prediction is shown as the dashed curve in Figure 12.

The direct measurements of  $\lambda_2$  were made in a similar way to those of  $\lambda_1$ . L2 was pulsed at a given random rate with 0.9 MeV pulses, while at the same time L1 and L2 were pulsed in coincidence at a low rate ( $\sim 100 \text{ s}^{-1}$ ) with a 1.8

**Figure 11**

The effective discriminator retrigger time calculated using equation 12a and the LET C oxygen data in Figure 10, and measurements of the effective discriminator up time in L2. Also shown is a second-order polynomial fit to the up-time measurements. If one assumes that the  $\tau_{\text{retrig}}$  curve calculated from the L1 measurements, also applies to L2, then the difference in the curves is the effective L2 dead time.

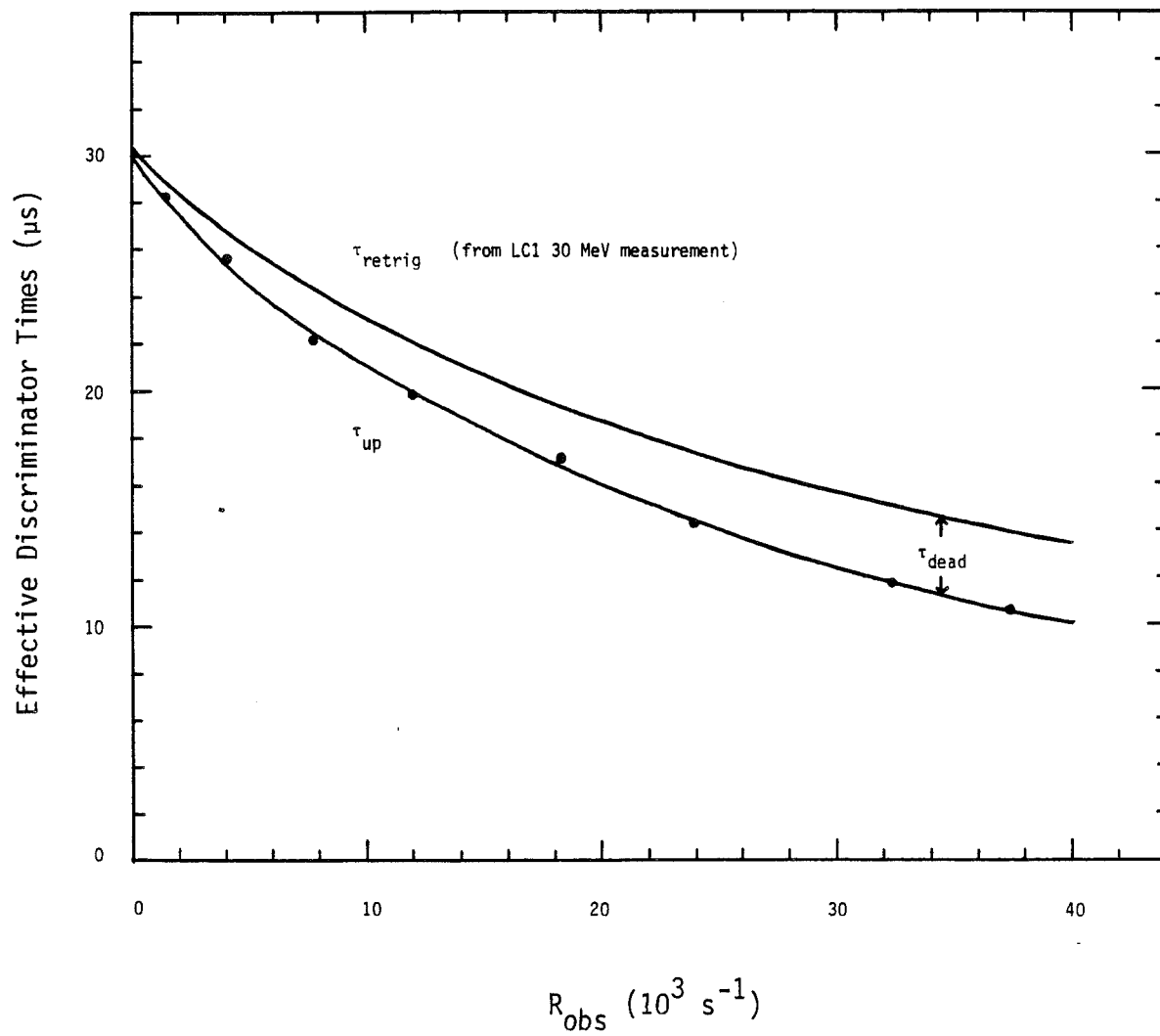
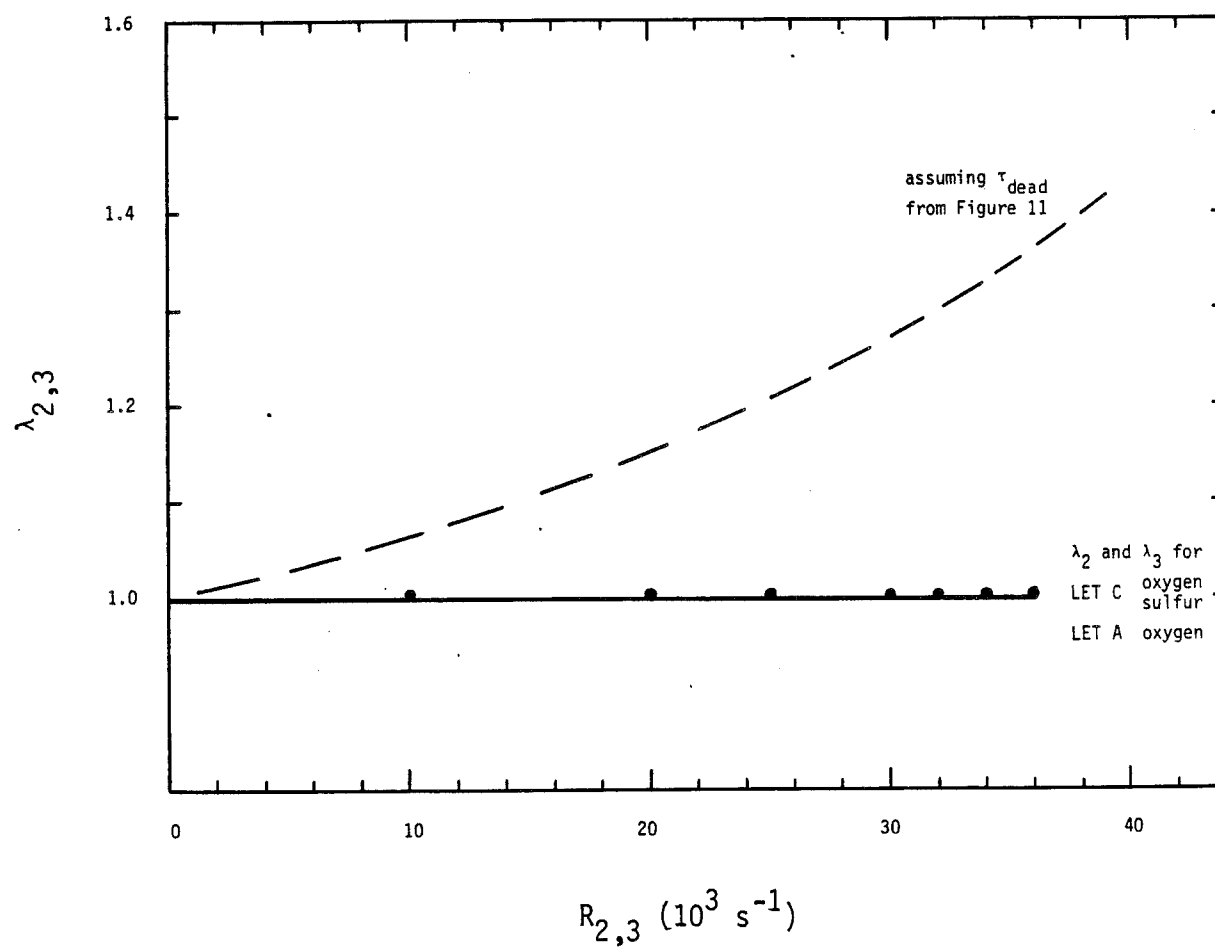


**Figure 12**

Measurements of the L2 and L3 livetime correction factors,  $\lambda_1$  and  $\lambda_2$ , for oxygen and sulfur nuclei as a function of the L2 and L3 singles rates of 0.9 MeV pulses (protons). All data are consistent with a livetime correction factor of 1.0. The dashed line was calculated with equation 12b using the  $\tau_{\text{dead}}$  in Figure 11 and  $\tau_{\text{strobe}}=4 \mu\text{s}$ .



MeV pulse in L1 and a large pulse in L2. The pulse height of the large pulse in L1 was chosen to be typical of either oxygen (30 MeV) or sulfur (90 MeV). The value of  $\lambda_2$  was determined from the fraction of coincidence events that were being counted in the LZ3 rate (L1-L2 command state). The exact same technique was used to measure  $\lambda_3$ , but with the former L2 pulses now going to L3 and the former L1 pulses to L1 and L2. Also, the instrument state was changed to L1-L2-L3, and the oxygen and sulfur pulses were now equivalent to L3 energy losses of approximately 200 and 600 MeV respectively. The measured  $\lambda_2$  and  $\lambda_3$  for LET C oxygen and sulfur and LET A oxygen are shown in Figure 12. All results are consistent with  $\lambda_2$  and  $\lambda_3$  equal to 1.0 (i.e. no livetime correction), for all values of the observed L2 and L3 rates! This represents the fact that, for all measurements, the LZ3 rate was the same as the L1 rate to within ~2%. The result is surprising both in terms of the prediction and in terms of our basic understanding of the discriminator characteristics. Even if the estimate of  $\tau_{\text{dead}}$  in Figure 11 was incorrect and the dead time was in fact zero, one would still expect  $\lambda_2 = 1/(1 - \tau_{\text{strobe}} R_2)$  due to the events with a timing as shown in Figure 7b<sub>3</sub>, which would give  $\lambda \approx 1.2$  for  $R_2 = 4 \times 10^4 \text{ s}^{-1}$ .

To further investigate, a repetitive double-pulse-type measurement was done. L1 and L2 were pulsed in coincidence with 1.8 and 30 MeV pulses respectively while a 0.9 MeV L2 pulse was moved back and forth in time with respect to them. In this way the various timing situations sketched in Figure 7b could be probed. It was found that, indeed, even in cases where the L2 discriminator was expected to be dead at the time of the strobe (Figure 7b<sub>2</sub>) or dead at the time of the event (Figure 7b<sub>3</sub>), a coincidence was established. The case where the L2 discriminator was dead at the time of the event was most peculiar because the coincidence event pulse in L2 was not retriggering the L2 discriminator in the sense of being counted in the L2 rate, and yet, with the L2 coincidence pulse

disconnected, the LZ3 rate dropped to zero. Measurements made by varying the relative timing of all three pulses indicate that the L2 discriminator behaves as sketched in Figure 13. A small pulse causes the first discriminator in all three figures, followed by a large pulse at a time indicated by the dashed vertical line. In Figure 13a the discriminator is retriggered normally. In 13b the large pulse occurs during the dead time, but somehow causes the discriminator to return to the up state for an additional  $\sim 6 \mu s$  without retriggering it. In Figure 13c the large pulse occurs near the end of the up time and causes the up time to be extended. In all cases the L1 strobe finds the L2 discriminator up, and the LZ3 rate is therefore incremented.

Although it may be difficult to parameterize and understand the discriminator behaviors that have been described in this subsection, the results are easy to use. The total livetime correction factor for the LZ3 rate for oxygen and sulfur is the product of the measured  $\lambda_1$ ,  $\lambda_2$ , and  $\lambda_3$ . Since  $\lambda_2$  and  $\lambda_3$  were found to be 1.0 as shown in Figure 12, only  $\lambda_1$  need be considered. Therefore, using oxygen as an example, equation 9 becomes

$$r_{oxy} = \frac{n_{pha-oxy}}{n_{pha-tot}} \lambda_1(R_1) LZ3_{obs} \quad (13)$$

where  $\lambda_1$  can be determined for the observed  $R_1$  from Figure 10.



**Figure 13**

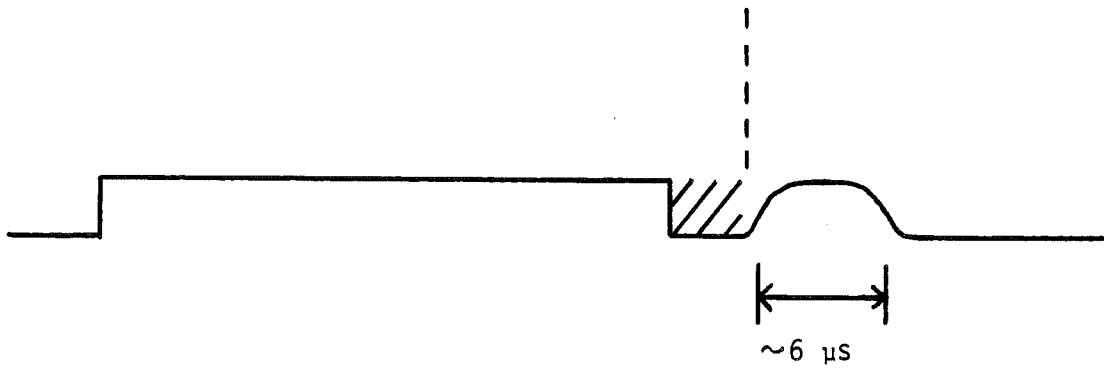
Peculiar discriminator outputs for the case of a small pulse followed by a large pulse. A 0.9 MeV pulse triggers the discriminator, and is followed by a 30 MeV pulse at a time indicated by the dashed line.

- a) Normal retrigger.
- b) The large pulse causes the discriminator to come up again without retriggering it.
- c) The large pulse causes the discriminator to stay up for an extra  $\sim 6 \mu s$ .

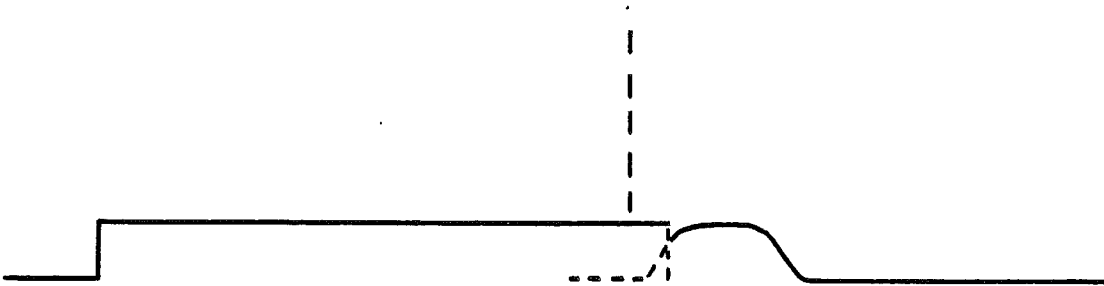
a)



b)



c)



### Slant Threshold Shifts

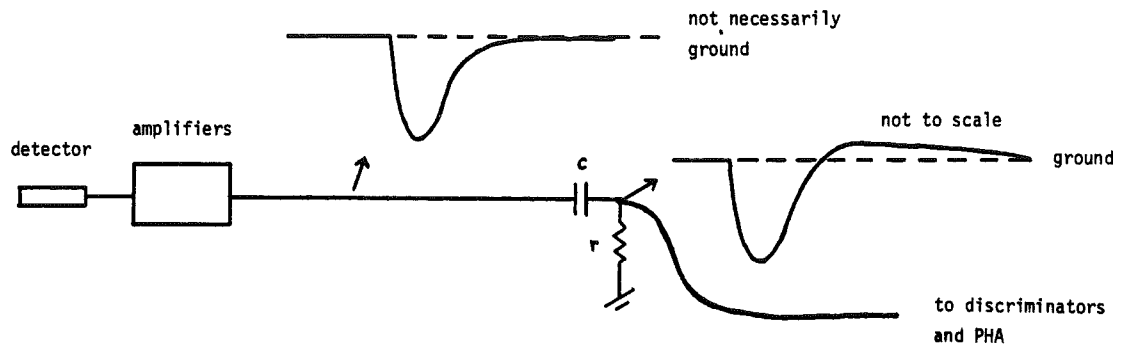
The outputs of the detector amplifiers are ac coupled to the discriminators and PHAs as shown in Figure 14a. One of the purposes of ac coupling is to insure a stable ground reference for the circuitry that follows. A consequence, however, is that pulses overshoot the nominal baseline before returning to it as indicated schematically in the figure. This overshoot can be understood in terms of the requirement that the long term average charge on the capacitor remain constant, and therefore that the total integral (ground = 0) of a pulse or group of pulses be zero. Figure 14b shows the approximate pulse shape for a 1 volt pulse (full scale = 10 volts) on two different scales. The overshoot is  $\sim 1\%$  of the pulse height and decays in  $\sim 1$  ms. Even though the overshoot is small, it can accumulate during high flux periods as shown in Figure 14c to cause a significant change in the effective baseline. For a constant rate, constant pulse size condition, the average baseline will settle at a value that makes the long term integral of the signal zero. A simple model relating the baseline shift to the average rate and pulse height of the incoming signal will be discussed later. As indicated in the figure, discriminator thresholds are set at constant values with respect to ground. Thus, when the baseline is shifted, larger pulses are required to trigger the discriminators than in the unshifted case. Since it is essential, when reporting particle fluxes, to specify the true energy threshold of the observation, an effort was made during the third calibration to determine the effective threshold of the slant discriminator for different rate and pulse-height conditions.

The measurements were made by applying given random rates and pulse sizes to L1, and at the same time pulsing L1 and L2 in coincidence at a low rate with various sized L1 pulses. (Pulse heights were measured and adjusted with

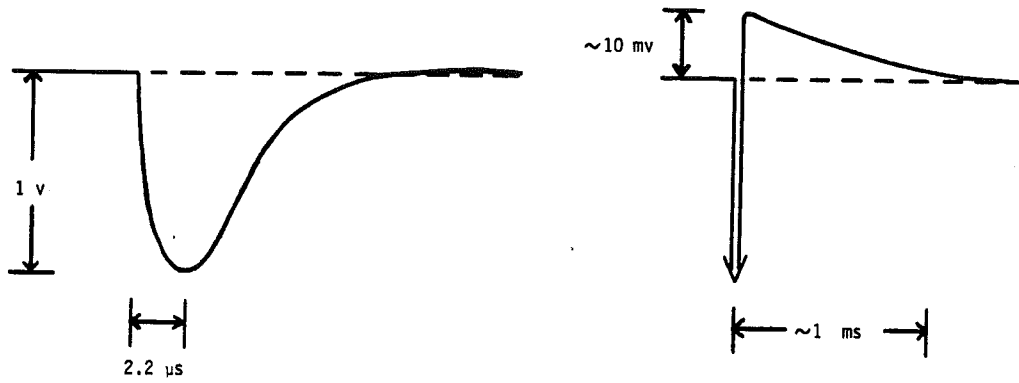
**Figure 14**

Illustrations of how a baseline shift occurs and how it can cause an increase in the effective threshold of a discriminator.

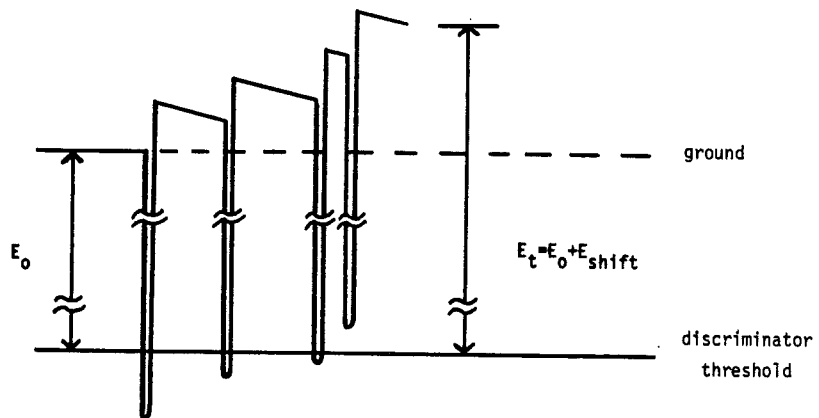
a)



b)



c)



the random pulses turned off and the baseline at ground since a baseline shift also shifts the pulse heights returned by the PHAs.) By monitoring either the LZ3 or LZ3\* rate (instrument in the L1-L2 command state), as a function of L1 pulse size, the effective slant threshold could be determined. For instance, if the random pulses triggering L1 were large enough to also trigger the slant, the LZ3\* rate was monitored. When the L1 test pulses were well below the slant threshold, a certain LZ3\* rate, LZ3\*<sub>0</sub>, was observed. The rate was generally close to the true input rate of the test pulses, but somewhat below it since some of the test pulses were not triggering L1 due to deadtime effects caused by the random pulses. The L1 test pulses were then increased in size. At some point the test pulses began to trigger the slant threshold and the LZ3\* rate decreased. For large enough pulses the LZ3\* rate dropped to zero. Both the one sigma turn-on width of the threshold,  $\sigma_t$ , and its mean value,  $E_t$ , defined by the level at which 50% of the pulses trigger it, could be easily determined from a probability plot of LZ3\*/LZ3\*<sub>0</sub> as a function of test pulse size. For the case where the random pulses were not large enough to trigger the slant, LZ3 was monitored instead of LZ3\*. Figure 15 shows the slant threshold probability plots for three different rates of oxygen-sized pulses (~30 MeV). The measurements are consistent with straight lines, indicating that the turn-on profile is approximately gaussian. Specifically, it will be assumed that the probability, P, of a particle with energy loss E in L1, triggering the threshold is

$$P(E, E_t, \sigma_t) = \frac{1}{2} \left[ 1 + \operatorname{erf} \left( \frac{E - E_t}{\sqrt{2} \sigma_t} \right) \right] \quad (14)$$

where erf is the error function and  $E_t$  and  $\sigma_t$  are the measured threshold and width. The measured values of  $E_t$  and  $\sigma_t$  for several input rates and pulse heights are listed in Table 5. Both the observed and true rates are given. Note

**Figure 15**

Probability plot of the fraction of test pulses triggering the slant threshold as a function of pulse height. Data is shown for baseline shifts caused by three different observed rates of 30 MeV pulses.

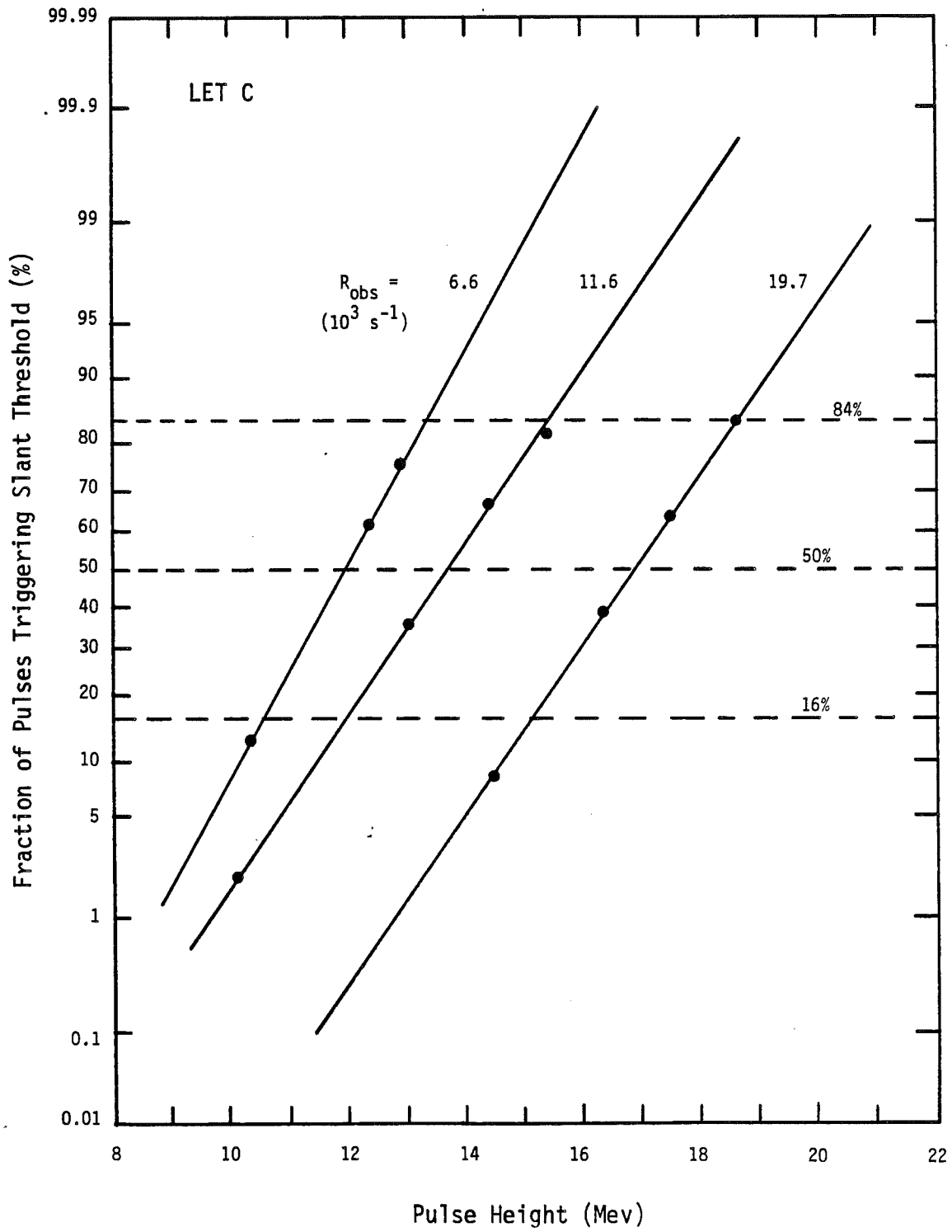




TABLE 5

Slant Threshold Shifts

$R_{\text{obs}}$ ( $10^3 \text{ s}^{-1}$ )	$R_{\text{true}}$ ( $10^3 \text{ s}^{-1}$ )	Pulse Height (MeV)	Energy-Loss Deposition Rate ( $10^5 \text{ MeV s}^{-1}$ )	$E_t^*$ (MeV)	$\sigma_t$ (MeV)	$E_{t\text{-eff}}^*$			
						Oxygen		Sulfur	
						$\gamma=5$	$\gamma=1.1$	$\gamma=5$	$\gamma=1.1$
						(MeV/nuc)	(MeV/nuc)	(MeV/nuc)	(MeV/nuc)
6.6	7.2	7.5	0.54	10.2	0.3	1.08	1.08	0.86	0.86
11.6	14.1	7.5	1.06	10.7	0.5	1.10	1.10	0.87	0.88
6.6	7.2	15.4	1.11	11.2	1.1	1.12	1.13	0.89	0.89
19.7	28.7	7.5	2.15	11.3	0.5	1.14	1.14	0.90	0.90
11.6	14.1	15.4	2.17	12.4	1.1	1.19	1.20	0.93	0.94
6.6	7.2	30.8	2.22	11.9	1.4	1.16	1.18	0.91	0.92
11.6	14.1	30.8	4.34	13.7	1.7	1.26	1.28	0.97	0.98
19.7	28.2	15.4	4.34	14.3	1.2	1.30	1.31	1.00	1.00
6.6	7.2	92.3	6.65	14.0	2.8	1.24	1.28	0.96	0.99
19.7	27.8	30.8	8.56	16.9	1.7	1.45	1.46	1.08	1.09
11.6	14.1	92.3	13.01	17.6	3.2	1.44	1.50	1.08	1.11

\* The nominal threshold is 9.6 MeV. For  $E_t=9.6$  MeV and  $\sigma_t=0$ , the effective thresholds for oxygen and sulfur nuclei are 1.06 and 0.85 MeV/nuc respectively.

that measurements were made only for relatively large pulses, even though L1 was predominately triggered by small pulses ( $\sim 1$  MeV) in the Jovian magnetosphere. This is because it was observed during the calibrations (and makes sense considering the ac coupling) that the shift due to the small pulses was less than  $\sim 1$  MeV, while the objective of the measurement was to determine the conditions for which shifts of several MeV occur.

Instead of quoting thresholds in terms of average values and widths, one usually quotes an effective threshold,  $E_{t-\text{eff}}$ , defined as the threshold that a "perfect" zero-width discriminator counting at the same rate as the actual discriminator, would have, i.e.,

$$\int_{E_{t-\text{eff}}}^{\infty} \frac{dJ}{dE} dE = \int_0^{\infty} \frac{dJ}{dE} \frac{1}{2} \left[ 1 + \operatorname{erf} \left( \frac{E - E_t}{\sqrt{2}\sigma_t} \right) \right] dE \quad (15)$$

where  $\frac{dJ}{dE}$  is the differential intensity. This effective threshold has been calculated for the measured  $E_t$  and  $\sigma_t$  assuming  $\frac{dJ}{dE} \propto E^{-\gamma}$  for a wide range of  $\gamma$ 's. In these calculations, the energy loss in the telescope window has also been included in the argument of the error function so that the resulting thresholds apply to the energy of the particles prior to their entering the telescope. The effective thresholds for oxygen and sulfur nuclei for  $\gamma=5$  and  $\gamma=1.1$  are listed in Table 5. The differences in the results for the two values of  $\gamma$  are small, indicating that the effective threshold, not including the window energy loss, is not substantially different from  $E_t$ . For oxygen the energy loss in the window is almost as large as the slant threshold, so that a factor of  $\sim 2$  shift in the threshold causes a factor of  $\sim 1.5$  shift in  $E_{t-\text{eff}}$ . For sulfur, the energy loss in the window is twice as large as the slant threshold, so that the largest shift in  $E_{t-\text{eff}}$  is only  $\sim 25\%$ .

A model will now be developed to estimate the magnitude of the baseline shift for a given input rate and pulse height. In order to simplify the problem, it will be assumed that the rate is constant, that the pulses are evenly spaced in time, and that the pulses are rectangular in shape. This situation is shown in Figure 16a. The baseline is shifted somewhat to equalize the area above and below ground. Between pulses the overshoot decays exponentially toward ground with the  $rc$  time constant of the ac coupling (see Figure 14a). If one further assumes that the rate is high enough to neglect the decay between pulses ( $1/R \ll rc$ ), then Figure 16b applies. The pulse width is  $t_p$ , the height is  $h$ , and the baseline shift is  $b$ . In order to have equal areas above and below ground,

$$t_p (h-b) = \left( \frac{1}{R} - t_p \right) b$$

or

$$b = R h t_p \quad (16)$$

A more careful derivation including the overshoot shown in Figure 16a gives

$$b = R h t_p e^{-\left(\frac{1}{R} - t_p\right)/rc} \quad (17)$$

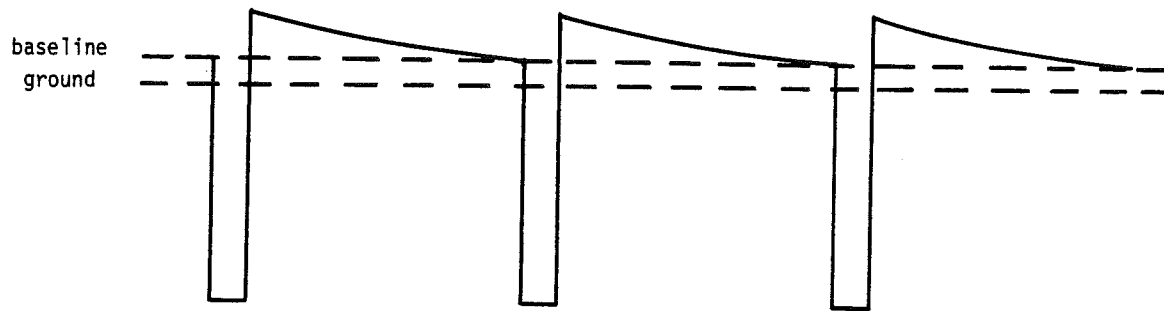
which, for  $1/R - t_p \ll rc$ , reduces to equation 16. Since  $rc \approx 0.5$  ms and  $t_p \approx 5$   $\mu$ s, one would expect equation 16 to hold for  $R \gg 2 \times 10^5$  s<sup>-1</sup>. Table 5 indicates that this condition is approximately valid ( $R \approx R_{true}$ ) for the measured data, so that the data can easily be compared to the model. The quantity  $R \cdot h$  is the energy-loss deposition rate in L1 and is listed in Table 5. In Figure 17  $E_t = b + 9.6$  MeV is plotted as a function of this quantity for the measurements listed in the table. The solid curve is a second-order polynomial fit to the data and the dashed line is calculated with equation 16, using  $t_p = 5$   $\mu$ s. Considering the approximations

**Figure 16**

Idealized amplifier outputs for evenly spaced, constant sized pulses.

- a) The baseline decays exponentially toward ground between pulses.
- b) The rate is high enough that, to first approximation, no decay occurs between pulses. This figure is used to calculate the baseline shift in terms of the pulse height, width, and rate.

a)



b)

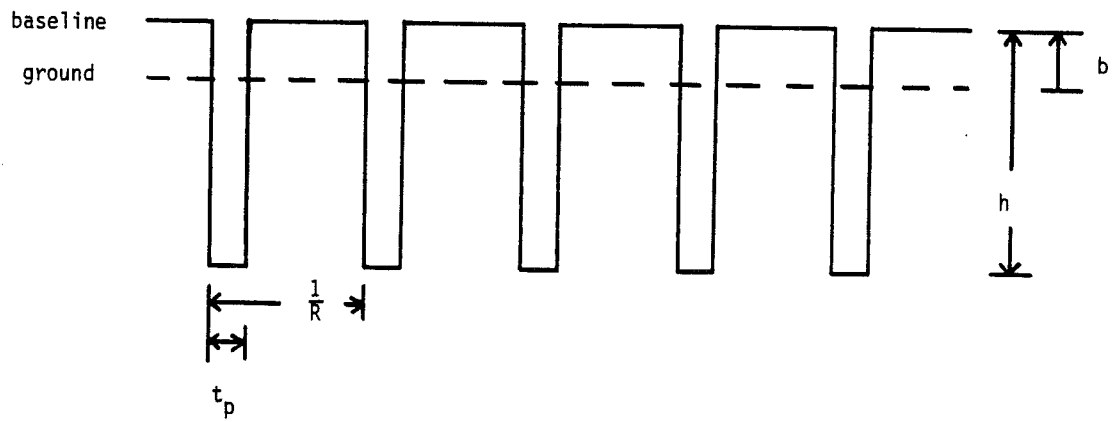
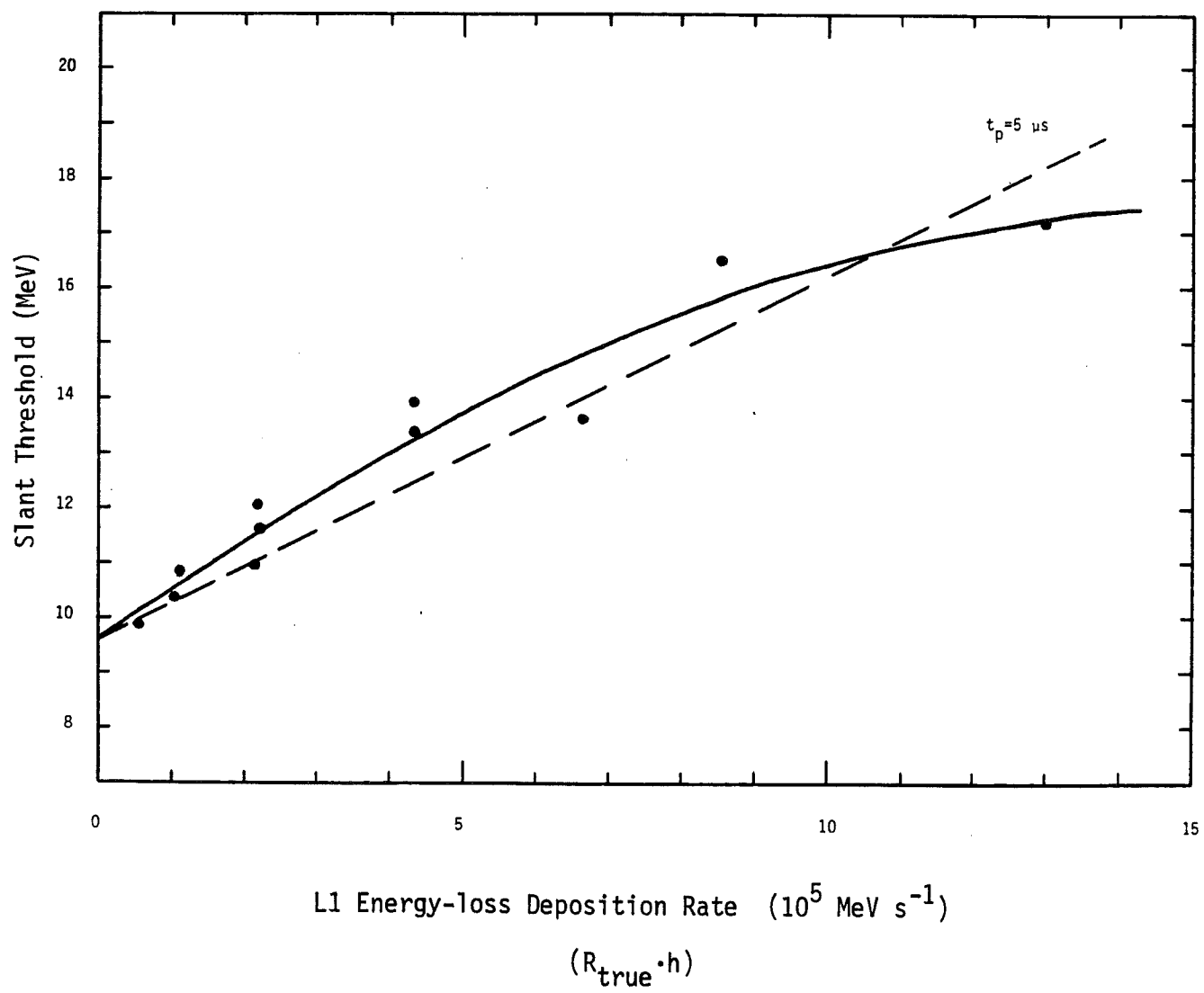


**Figure 17**

Measurements of the slant threshold shift as a function of the L1 energy-loss deposition rate. The data are also listed in Table 5. The solid line is a second-order polynomial fit to the data, and the dashed line is calculated from the model (equation 16 with  $t_p=5\ \mu s$ ). The nominal slant threshold is 9.6 MeV.



that were made in the model, the agreement with the data is quite good.

### Rate Decreases Caused by Heavy-ion Flux Increases

In the discussion of Table 2 and Figure 9 it was noted that, for some pulse sizes and rates, the observed rate (discriminator triggering rate) actually decreases toward higher true rates. This rollover in the instrument response is most likely due to saturation effects in the discriminator circuitry. There are many other mechanisms that can lead to rollovers <sup>†</sup>. During the calibrations another such mechanism was found that may explain some peculiar features that were seen in the LET counting rates in the Jovian magnetosphere. The basic idea concerns a discriminator that is predominantly being triggered by small, near-threshold pulses. If a few large pulses are then added, an average baseline shift occurs, moving some of the small pulses below the threshold. Since the large pulses do not contribute significantly to the discriminator counting rate, the rate decreases.

Measurements of this effect were made by simply pulsing L1 with a high rate of small pulses and then monitoring the L1 rate while various rates of large pulses were added. Figure 18 shows the measured L1 rate as a function of the rate of large pulses,  $R_{big}$ , for 30 MeV (oxygen) and 90 MeV (sulfur) pulses. The small pulses were 0.9 MeV (protons) and were applied at a true rate of  $2.4 \times 10^6 \text{ s}^{-1}$  for all measurements. Using the 90 MeV curve as an example, it is seen that  $R_{big}$  can be divided into three regions where different effects dom-

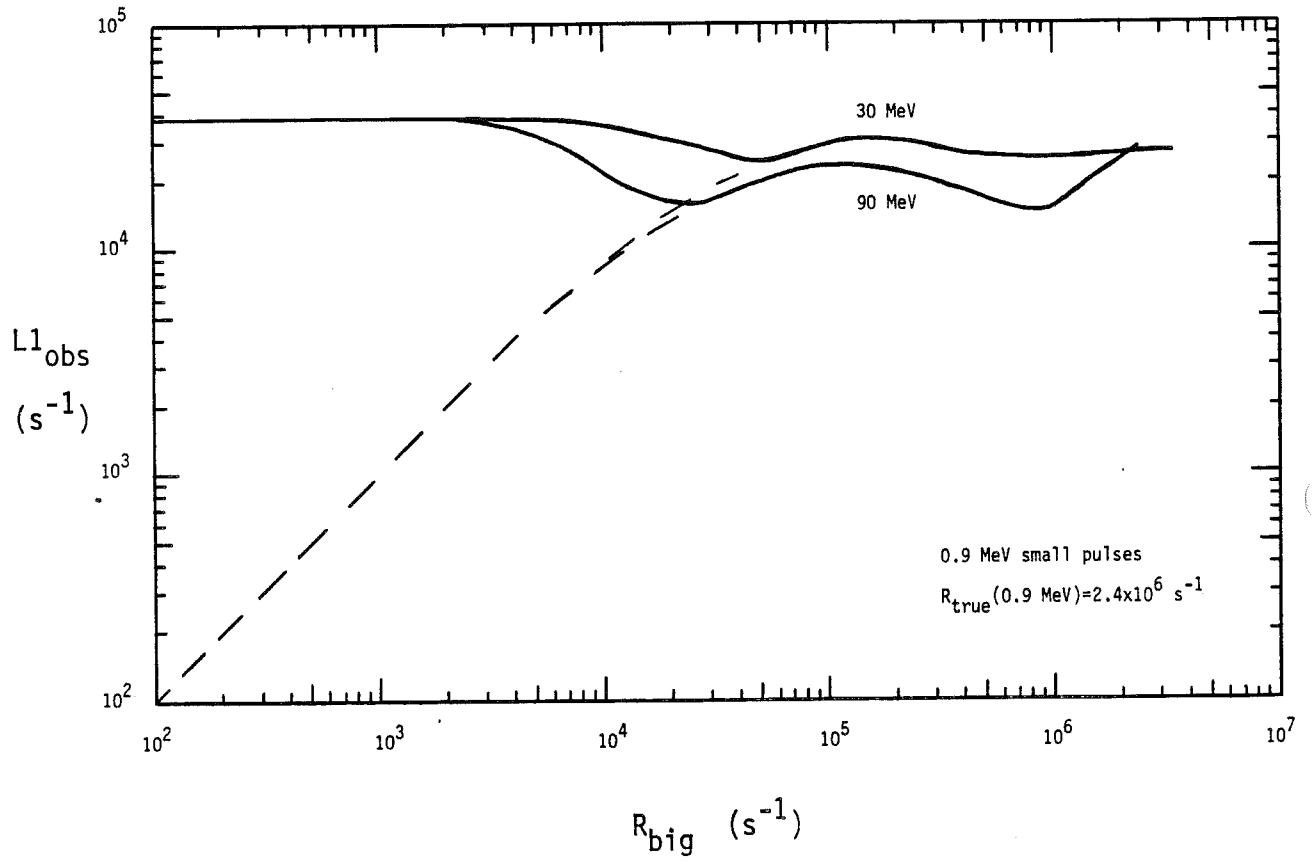
---

<sup>†</sup> A famous example of a rollover is the case of the University of Iowa cosmic ray investigation on Explorer I and III (Van Allen, 1959). The realization that the responses of the geiger tubes in the instruments were severely rolled over due to large particle fluxes led to the discovery of the Van Allen trapped radiation belts. In this case the effect was due to blanking of the geiger tubes (Van Allen *et al.*, 1958).



**Figure 18**

The observed L1 rate as a function of the true input rate of 30 and 90 MeV pulses, for a true input rate of 0.9 MeV pulses of  $2.4 \times 10^6 \text{ s}^{-1}$ . The dashed lines indicate what  $L_{1\text{obs}}$  would be if the 0.9 MeV pulses were turned off.



inate:

- 1)  $R_{big} < 2 \times 10^3 \text{ s}^{-1}$  — The baseline shift due to the 90 MeV pulses is not large enough for a significant number of the 0.9 MeV pulses to be below threshold, and therefore  $L1_{obs}$  remains at  $\sim 4 \times 10^4 \text{ s}^{-1}$ .
- 2)  $2 \times 10^3 < R_{big} < 2 \times 10^4 \text{ s}^{-1}$  — The baseline shift is large enough to cause increasing numbers of 0.9 MeV pulses to be below threshold and  $L1_{obs}$  decreases. If the 0.9 MeV pulses caused no shift of their own and if they were each distinct pulses (i.e. no pile-up), then one would expect all of them to fall below threshold for baseline shifts greater than 0.7 MeV ( $L1$  threshold = 0.2 MeV). Figure 17 shows that, for 90 MeV pulses, the baseline shift reaches 0.7 MeV for  $R_{big} \approx 2 \times 10^3 \text{ s}^{-1}$ , so that, in the simplest approximation, one would expect the  $L1$  rate to drop steeply for  $R_{big} > 2 \times 10^3 \text{ s}^{-1}$ .  $L1_{obs}$  does in fact start decreasing above this rate, but the decrease is gradual, indicating that there is significant pile-up of the 0.9 MeV pulses as expected for an input rate of  $2.4 \times 10^6 \text{ s}^{-1}$ . A similar argument indicates that the 30 MeV pulses should cause decreases for  $R_{big} > 5 \times 10^3 \text{ s}^{-1}$ . The observed decrease starts at a somewhat higher rate of  $\sim 8 \times 10^3 \text{ s}^{-1}$ .
- 3)  $R_{big} > 2 \times 10^4 \text{ s}^{-1}$  — The  $L1$  rate has decreased to such an extent that the large pulses themselves dominate the rate. The qualitative shape of the curve is therefore similar to that of the 123 MeV curve in Figure 9.

The actual situation in a magnetosphere is not as simple as that simulated during the calibration, since the proton rate will not in general remain constant while the heavy-ion rate changes. The basic idea of a heavy-ion induced roll-over can, however, be used to qualitatively understand the  $L1$  rate profile in the Jovian magnetosphere. Figures 19 a and b show the observed  $L1$ ,  $SL$ , and  $L2$  rates as functions of time, near closest approach to Jupiter of Voyagers 1 and 2 respectively. The Voyager 1 data were obtained with LET B, and the Voyager 2

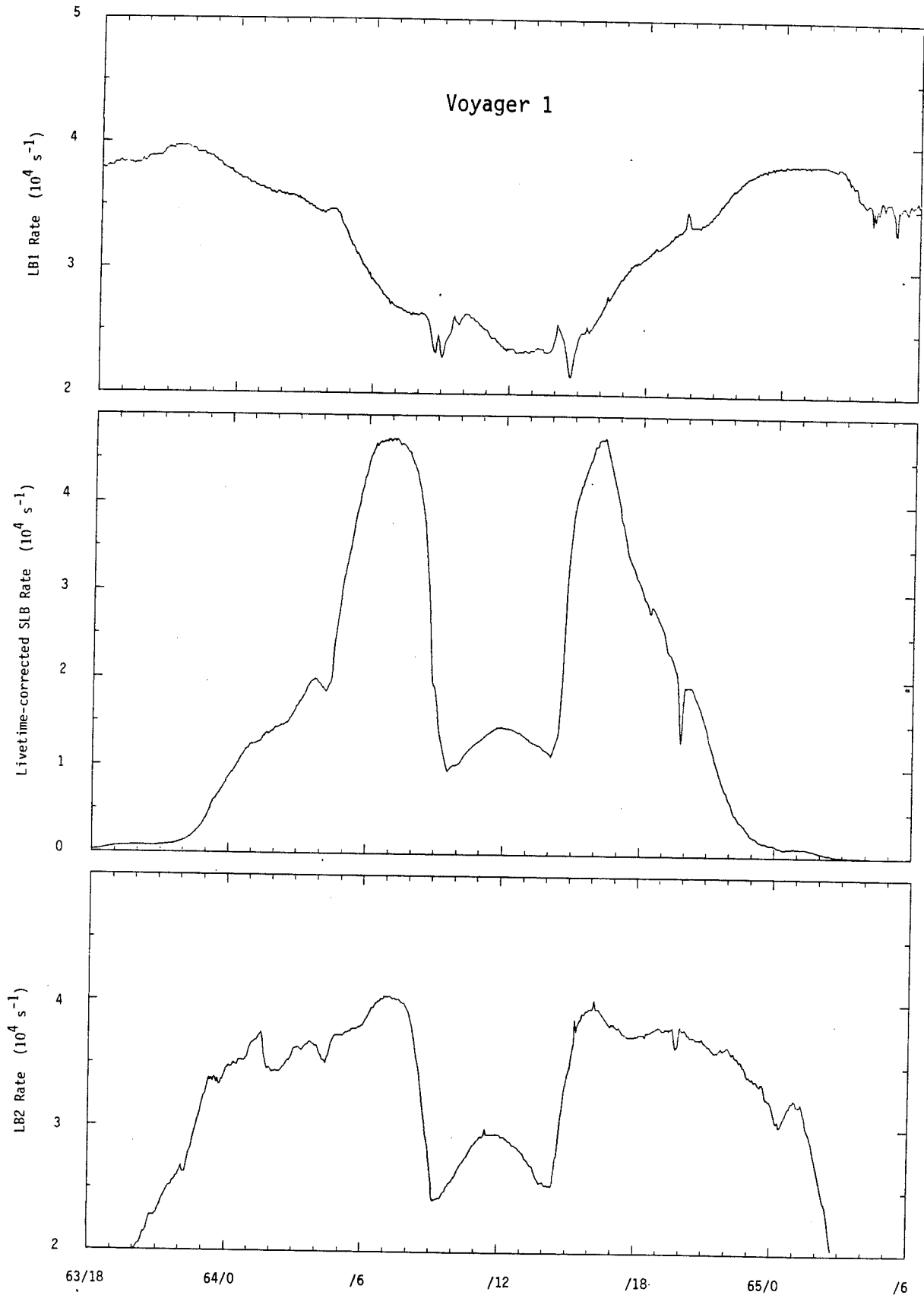
**Figure 19**

Observed L1, SL, and L2 rates in the Jovian magnetosphere. The SL rate has been livetime corrected using the data in Table 2.

a) Voyager 1

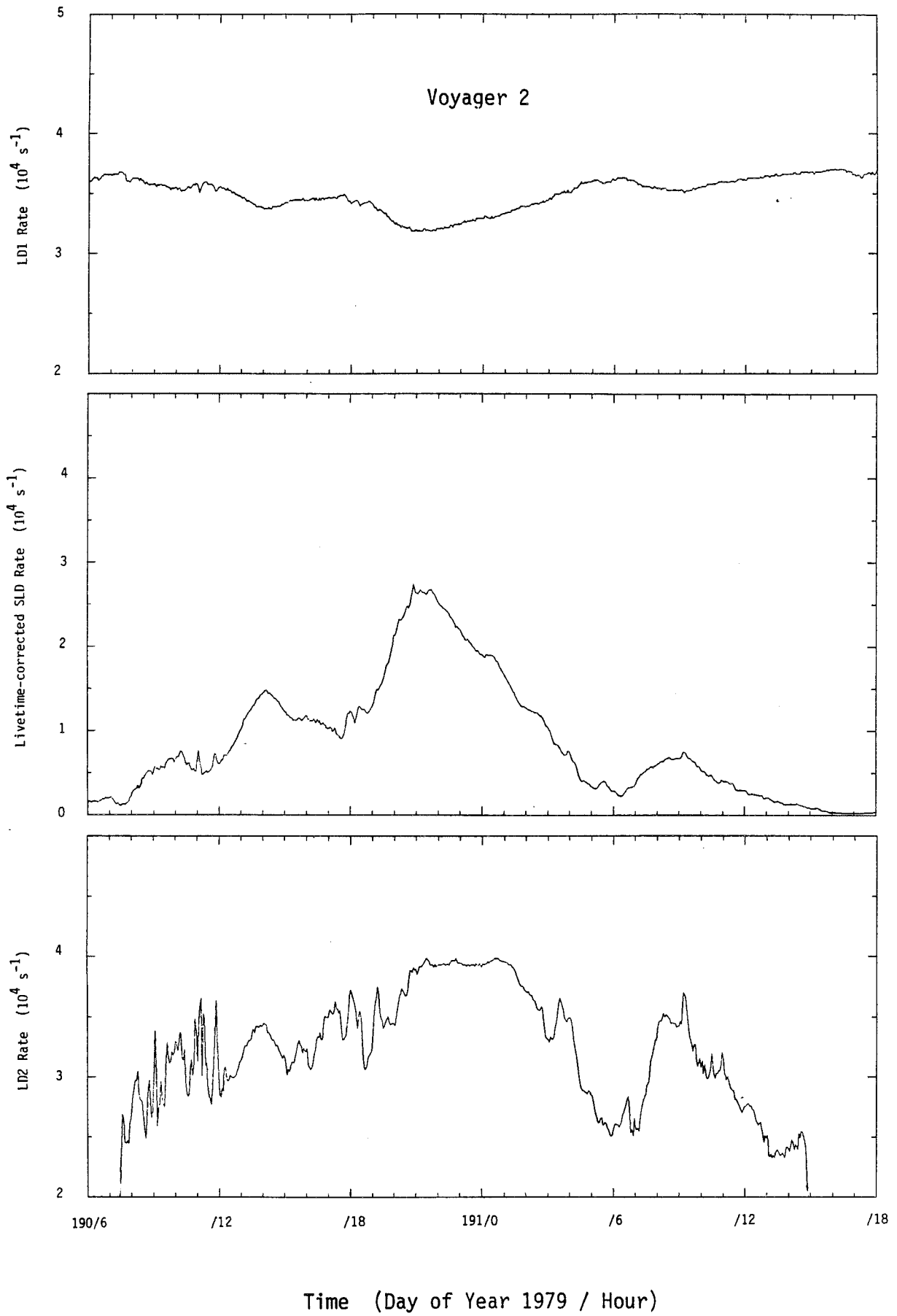
b) Voyager 2

a)



Time (Day of Year 1979 / Hour)

b)



data with LET D. The SL rate has been corrected for deadtime effects using the data in Table 2, and therefore represents the true heavy-ion rate. Throughout the time periods shown, the average energy loss of particles triggering the slant is between 15 and 20 MeV, except from 64/4 to /18 for Voyager 1, during which time the average energy loss increases and separates into peaks near 30 and 90 MeV. The minima in the Voyager SL rate at ~64/4 and ~64/20 are due to particle absorption by the Jovian moon, Europa, and the deep minima at ~64/9 and ~64/14 are due to absorption by Io and its plasma. The expected heavy-ion contribution to the L2 rate is less than a tenth of the SL rate, so that the L2 rate profile shown in the bottom panel is due almost entirely to protons and piled-up electrons. If the L2 rate could be accurately lifetime corrected, it would most likely have a similar profile to that of the SL rate. Neglecting heavy-ion rollover effects, one would expect the L1 rate to be saturated at  $\sim 4 \times 10^4 \text{ s}^{-1}$  throughout the time period shown, except near Io where the profile might be similar to that of the L2 rate. The actual L1 rate shown in the upper panel demonstrates that the heavy ions cause a substantial rollover. The effect is particularly noticeable at 64/7, /12, and /16, where the L1 rate dips down while the SL and L2 rates reach maxima. Note also that the Europa absorption features in the SL rate cause inverted features in the L1 rate.

Turning now to the Voyager 2 figure, we see that the maximum SL rate is less than that of Voyager 1, due mostly to the fact that Voyager 2 closest approach distance to Jupiter was  $\sim 10$  Jovian radii ( $R_J$ ) compared to  $\sim 5 R_J$  for Voyager 1. Also, for this reason, the absorption features of Europa ( $9.4 R_J$ ) and Io ( $5.9 R_J$ ) are not seen. The large-scale variation in the rate is due predominantly to varying spacecraft magnetic latitude. The L2 rate is much more irregular than the SL rate, but does have maxima at the times of the SL rate maxima. The L1 rate again has inverted features caused most likely by the

heavy ions. The rollover is less than for Voyager 1 since the SL rate is less and is dominated by smaller pulses. Note again that small irregularities in the SL rate (for instance at 190/11) appear inverted in the L1 rate.

More calibration measurements would be required to quantitatively understand the L1 rate in these regions. However, the calibration measurements and spacecraft data presented in this section do point out that care must be taken when interpreting dips and peaks in the counting rate of a single discriminator when heavy-ion fluxes are not known.



## Appendix

In this appendix, some detailed information about the LED calibration technique is presented. The LED - detector configuration that was used in the second and third calibrations is shown in Figure A-1. The detector and LEDs were enclosed in a box to eliminate room light interference and to facilitate keeping the detector in a dry nitrogen environment. The calibration detectors were substituted for the detectors in the telescopes of the spare CRS instrument by changing connectors at the pre-amplifier inputs. Several LEDs were suspended at a distance of  $\sim 1.5$  cm above the gold side of each calibration detector. (The gold side was found to be more light sensitive than the aluminum.) The type of LED that was used was the HP red high intensity LED (HP 5082-4658) because of its availability, high luminance, and focused beam. The beam has a FWHM of  $\sim 35^\circ$  so that at 1.5 cm, most of the light hits the detector. Red was chosen over green and orange because it was found to produce bigger signals in the detector for a given driving voltage and pulse width.

The LEDs were each pulsed by a fast square-wave pulse generator (III PG-33 or Chronetics PG-12). Table A-1 lists the signal sizes at the output of the detector amplifiers for several pulse widths and heights of the pulser. The induced signal size for a given driving pulse varied considerably from LED to LED due to both mounting differences and intrinsic differences in the LEDs, but this was not a problem since the size of the amplifier signal could be directly measured and adjusted to any desired value using either the instrument PHAs or an oscilloscope. The LEDs were quite dependable in that, even after many hours use over the period of a year, none of the  $\sim 10$  that were in the calibration boxes broke.

Random light pulses were produced by triggering the fast pulsers with ran-

*~10-100 ns  
~ 1 V  
adjust  
either*

**Figure A-1**

Sketch of the detector - LED configuration for the second and third calibrations.

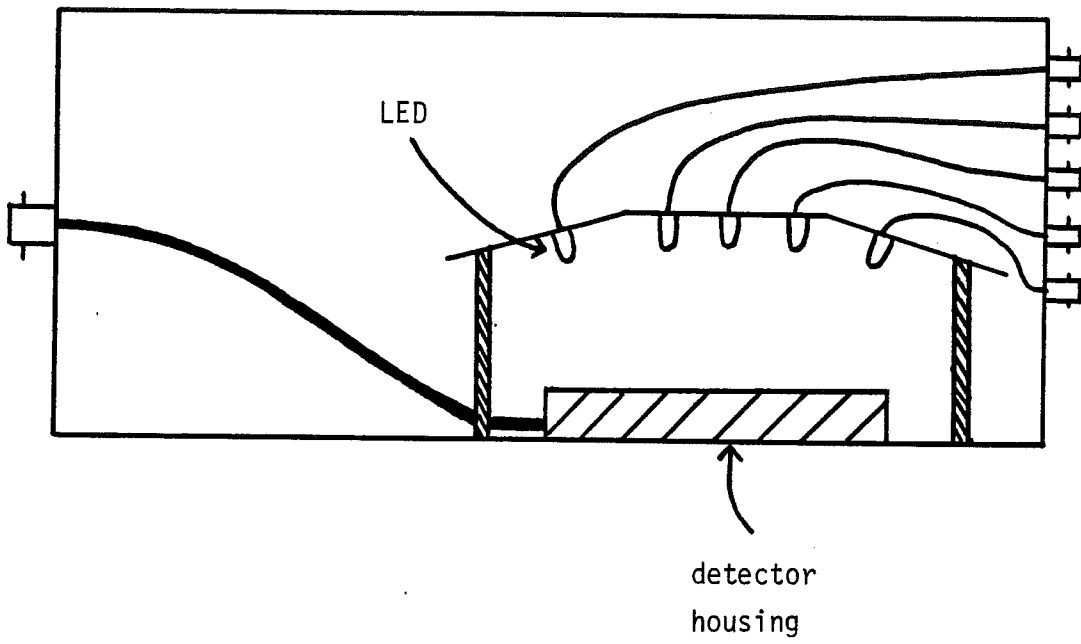


TABLE A-1  
Amplifier Output for Different Widths  
and Heights of Pulses into the LEDs

input pulse width (ns)	input pulse height (volts)	amplifier output* (volts)	equivalent particle $\Delta E$ in L1† (MeV)
8	4	0.03	0.9
8	8	0.2	6.1
50	4	1.0	31
50	8	5.0	154

\* full scale = 10 volts

† full scale = 307 MeV

dom signals. For the second calibration Berkeley Nucleonics DB-2 random pulse generators were used for triggering. For the third calibration a  $^{137}\text{Cs}$  69 mCi source (obtained from the Radiation Safety office) was used with lab scintillators and photomultiplier tubes to trigger EG&G fast discriminators which, in series with EG&G scalar drivers, triggered the fast pulsers. Several measurements that were made with both the random pulse generators and with the radioactive source were in good agreement.

### References

- Evans, R. D. 1955, *The Atomic Nucleus*, McGraw-Hill, New York.
- Gehrels, N., Stone, E. C., and Trainor, J. H. 1981, *J. Geophys. Res.*, submitted.
- Stilwell, D. E., Davis, W. D., Joyce, R. M., McDonald, F. B., Trainor, J. H., Althouse, W. E., Cummings, A. C., Garrard, T. L., Stone, E. C., and Vogt, R. E. 1979, *IEEE Trans. on Nuclear Sci.*, **NS-26**, 513.
- Stone, E. C., Vogt, R. E., McDonald, F. B., Teegarden, B. J., Trainor, J. H., Jokipii, J. R., and Webber, W. R. 1977, *Space Sci. Rev.*, **21**, 355.
- Van Allen, J. A. 1959, *Scientific American*, **200**, No. 3, 39.
- Van Allen, J. A., Ludwig, G. H., Ray, E. C., and McIlwain, C. E. 1958, *Jet Propulsion* **3**, 588.
- Vogt, R. E., Cook, W. R., Cummings, A. C., Garrard, T. L., Gehrels, N., Stone, E. C., Trainor, J. H., Schardt, A. W., Conlon, T., Lal, N., and McDonald, F. B. 1979a, *Science*, **204**, 1003.
- Vogt, R. E., Cummings, A. C., Garrard, T. L., Gehrels, N., Stone, E. C., Trainor, J. H., Schardt, A. W., Conlon, T. F., and McDonald, F. B. 1979b, *Science*, **206**, 984.

Note added by ECS

Table 4

Retrigger time depends on pulse size

A is the 1<sup>st</sup> pulse (75 keV/channel)

B is the 2<sup>nd</sup> pulse (75 keV/channel)

note if 2<sup>nd</sup> pulse is small, there is a longer  
retrigger time

but by 1.5 MeV pulse (B), the retrigger time  
is 20 - 30  $\mu$ s